ABSTRACT

Title of Thesis: MOLECULAR DYNAMICS SIMULATIONS OF LASER

INDUCED SHOCK RESPONSE IN REACTIVE Ni/Al

NANOLAMINATES

Degree Candidate: Alexander Blacque Meissner

Degree and Year: Master of Science, 2009

Thesis Directed by: Professor Michael Zachariah
                           Departments of Mechanical Engineering and Chemistry

To characterize the self-propagating, high-temperature exothermic alloying reactions of Ni/Al nanoscaled multilayered films induced by laser pulse shock loading, classical molecular dynamics simulations were performed. In the current work, a novel technique was developed to facilitate the energy input and distribution into nanolaminate thin films. The laser pulse shock loading technique enables the initial shock response of the material to be captured as well as the late-time mass diffusion controlled alloying reaction and Ni_3Al formation. Shock compression raises the temperature, pressure, and density of the Ni and Al layers which triggers the Ni to diffuse into the Al and initiate the self-propagating alloying reaction. Thermodynamic states, enthalpy of reaction, and global reaction rates of the laminated films were obtained. It was determined that the series of complex rarefaction and reflection waves play a significant role in altering the

thermodynamic state of the laminate. Attributes of the rarefaction and reflection waves are controlled by the geometry and thickness of the alternating layers. The dependence of layer thickness on the temperature, pressure, enthalpy of reaction, and global reaction rate was investigated and characterized.

MOLECULAR DYNAMICS SIMULATIONS OF LASER INDUCED

SHOCK RESPONSE IN REACTIVE Ni/Al NANOLAMINATES

Alexander Blacque Meissner

Thesis submitted to the Faculty of the Graduate School of the
University of Maryland, College Park in partial fulfillment
of the requirements for the degree of
Master of Science
2009

Advisory Committee:
Associate Professor Michael Zachariah, Chairman/Advisor
Associate Professor Gregory Jackson
Assistant Professor Santiago Solares

Dedicated to my wife, Christy,

who I am forever indebted to for her support.

and to my twin sons, Jack and Charlie,

who have inspired me to be a better man.

TABLE OF CONTENTS

LIST OF TABLES

LIST OF FIGURES

NOMENCLATURE

$A_{Measured}$ A generic measurable property

$\langle A \rangle$ Time average of function A

a Species concentration

C Specific heat capacity

C_v Constant volume specific heat capacity

C_p Constant pressure specific heat capacity

C_s Specific heat capacity of a solid

C_l Specific heat capacity of a liquid

$C_{p,s}$ Constant pressure specific heat capacity of a solid

$C_{p,l}$ Constant pressure specific heat capacity of a liquid

D Diffusion coefficient

E Energy of an atom embedded in the host (crystal structure)

E_a Activation energy

E_k Kinetic energy

E_T Total energy (internal energy for isolated systems)

$\vec{F}$ Force

F_a The energy required to place an atom of type a into the electron cloud of the host.

H Enthalpy

H_{Prod} Enthalpy of product species

H_{Reac} Enthalpy of reactant species

$\bar{h}$ Enthalpy per mole

$\tilde{H}$ Hamiltonian

ΔH_m Enthalpy of fusion

ΔH_{RXN} Enthalpy of reaction

I Laser output intensity

I_0 Laser pulse intensity constant

i Atom index

j Atom index

k_0 Frequency factor

k_b Boltzmann's constant

m Mass

N Refractive index

n Number of atoms

P Pressure

P_{ref} Reference pressure

$\vec{p}$ Momentum vector

$\vec{p}^{\,N}$ A set of momentum vectors that lists the momentum of each atom

Q Distribution of transient absorbed energy density

R Universal gas constant

R_{sf} Surface reflectivity

r Scalar distance between two particles

r_c Cutoff radius

r_{Ni} Atomic radius of Ni

$\vec{r}$ Position vector

$\vec{r}^{\,N}$ A set of vectors that locate the atomic centers of mass

S_{ab} Stress Tensor

T Temperature

T_m Melting temperature

T_{Max} Maximum temperature

T_{ref} Reference temperature

T_{st} Surface transmittance

t Time

t_0 Initial time

t_p Laser pulse characteristic time

U Internal energy

$U_{P.E.}$ Potential energy

u velocity of combustion wave propagation

V Volume

v Velocity

v_0 Initial velocity

v_f Final velocity

Greek Symbols

a Represents an atom species

b Represents an atom species

d Absorption depth

e Lennard-Jones parameter

h Collision distance between two atoms' centers of mass

q_a The contribution to the electron charge density from an atom of type a

k Thermal conductivity

l Wavelength of the laser pulse

m Viscosity

m_∞ Asymptotic viscosity

r Density

s Lennard-Jones parameter

t A dummy time integration variable

f_{ab} Short-range pairwise potential function

c_{Ni} Ni concentration

y A function that accounts for the reaction rate's dependence on concentration

CHAPTER 1

INTRODUCTION TO INTERMETALLIC COMPOUNDS

1.0 Introduction

Intermetallic compounds are defined as solid phases containing two or more metallic elements, with optionally one or more non metallic elements, whose crystal structure differs from that of the other constituents [1]. Much attention is focused on studying intermetallic compounds due to their enhanced material properties and thus potential application for highly specialized machine applications. Self-propagating high-temperature synthesis (SHS) is a relatively new method of manufacturing intermetallic compounds. This relatively low cost manufacturing method has accelerated the widespread use of intermetallic compounds in the fields of commercial industry, aerospace, and defense. The SHS process is attractive to material manufacturers because it involves relatively simple equipment and requires low energy input and therefore drastically reduces the cost of production [2, 3]. It is known that the combustion synthesis of TiNi powders is used to produce sheets, tubes, and wires with shape memory characteristics [40] that will one day be integrated into commonly manufactured products such as automobiles and electrical circuit components. The high energy release and fast burn rates that are demonstrated by SHS of intermetallic compounds have potential for applications in the defense and aerospace industries. They show promise for underwater applications since the combustions temperature is extremely high and no additional oxidizer is needed for the reaction. These reactions do not produce gas products due to their condensed states. This makes them good candidates for applications that require low volume expansion such as propellants and initiators.

It is of particular interest to fully understand the reaction mechanisms behind the alloying process of intemetallics. Often, reaction mechanisms may be controlled to alter the characteristics of the global reaction so that a desired output in material properties is achieved. For example, the energy release rate, product species formation, and thermodynamic output can be influenced by controlling the reaction rates, combustion temperature, or combustion pressure of the synthesis process.

1.1 Current Research of Intermetallic Compounds

Currently, there is a fair amount of research in the field of intermetallic compounds. It is impractical to attempt to cover all research efforts involving intermetallics. The goal of this section is to introduce the reader to some general areas of research in the field. Combinations of experimental and simulation efforts have been carried out to acquire a deeper understanding of the complex physical and chemical processes that govern the behavior of intermetallic materials. Scores of experiments have been devoted to the investigation and study of thermodynamic properties and processes, diffusion processes, viscosity, mechanical properties, and effects of alloy composition. Although many aspects of intermetallic materials have been characterized by experimental efforts, many aspects of the fundamental physical and chemical processes that are involved with intermatallic compounds are largely unknown. Simulation, especially at the molecular and atomistic levels, offers unique insight into physical and chemical phenomenon of intermatallic materials.

1.1.1 Research of Thermodynamic Properties of Inermetallic Compounds

A fair amount of work has been done to develop simulation techniques that are able to characterize the thermodynamic and reaction behavior of these materials. Specifically, much attention has been dedicated to developing embedded-atom potentials (EAM) for metal alloy systems [6, 7, 8]. Embedded-atom potentials have been used in first-principles calculations to investigate thermodynamic properties of Ni, Al, NiAl, and Ni_3Al [9]. One study has used the EAM potential to study the vibration thermodynamic properties of ordered and disordered Ni_3Al [10]. The most common simulation technique that has been used to study the Ni/Al system is molecular dynamics with EAM potentials. Molecualar dynamics simulation methods have been used to investigate structural, thermodynamic, and atomic-transport properties of liquid Ni/Al alloys [11]. Simulations have been carried out to investigate the pressure dependence of melting temperatures of Al and Ni [12, 13]. Simulations have also been used to study the effects of pressure on reactive multilayer thin foil joining as well as other reactive materials [14, 15]. There is immense interest in the combustion of Ni and Al at the nanoscale. Molecular dynamics simulations have been performed to determine the combustion characteristics of Ni coated Al nanoparticles [16]. Several efforts, including this work, have focused on developing simulation techniques that allow for the investigation of shock induced diffusion-controlled, alloying reactions of intermetallic materials [17, 18, 19].

1.1.2 Research of Diffusion, Viscosity, and Alloy Composition of Inermetallics

Insight into the diffusion mechanisms of reactive alloy systems is essential for understanding the chemical reaction mechanisms of these systems. Experimental efforts have been conducted to obtain viscosity data of the liquid Ni/Al system [20-23]. In these

studies, the effect of Ni concentration on the viscosity has been examined in detail. Some

works have focused on calculating the diffusion coefficients from the viscosity data [21].

Other works have concentrated on calculating the diffusion coefficients using molecular

dynamics simulations [23]. Many works are centered on mathematical analytical

solutions to Fick's second law of diffusion with eroding material interfaces (Stefan

problems) [24-27]. It is the author's opinion that much is to be gained from further

studies of metallic alloy systems in the areas of diffusion, viscosity, and alloy constituent

concentrations.

1.1.3 Research of Mechanical Properties of Inermetallic Compounds

In addition to thermodynamic properties and reaction characteristics of

intermetallic systems, mechanical properties of intermetallics are also of great interest.

Some current research efforts of intermetallic mechanical properties deal with creep,

fatigue, solution and defect hardening, and strain hardening. Shah and Lee in [28]

dedicate a chapter to the assessment of our current understanding of creep behavior of

intermetallics and intermetallic-based multiphase alloys. The principal objective of their

work is to compare creep behavior of intermetallics with ordered structures, to that of

disordered materials, and bring forth any unique aspects that contribute to the

enhancement of creep resistance. Stoloff, also in [29], reported works concerned with

fatigue of intermetallic materials. In this work, the response of intermetallic compounds

to cyclic deformation is investigated. These works are particularly concerned with the

progression of fatigue damage during the early stages of cyclic loading and the influence

of numerous experimental and material variables on fatigue life and crack growth rates.

Fleischer, in [30], has researched solution and defect hardening of intermetallic

compounds. In this work some basic results in solid solution hardening of intermetallic compounds are summarized. Gray III and Pollock in [31] give an overview of the phenomenon of strain hardening in ordered intermetallic compounds.

1.2 Introduction to Combustion Synthesis of Intermetallic Compounds

Combustion synthesis is a manufacturing method used to create or produce materials, usually used in highly specialized machines such as turbine engines and aerospace applications. Self-propagating high-temperature synthesis (SHS) is the most commonly used combustion synthesis method. In this method, the product is created from an exothermic autowave reaction of the reactant species. The chemical reaction is initiated by heating a very small region, usually at the surface of a sample. Often, the sample is comprised to two or three metal powders that are premixed. The liberated chemical energy from the initial heated region is enough to initiate a reaction wave that propagates through the entire sample. Combustion synthesis of intermetallic compounds is a relatively new manufacturing method used for producing exotic metal alloys. Methods of producing intermetallics by combustion synthesis were first documented in 1970. Many conventional manufacturing methods have been used to produce intermetallics. Some examples include reactive sintering or reactive hot isostatic compaction, crystallizing molten metallic compounds by vacuum melting with directional cooling, and mechanical alloying followed by vacuum hot pressing [32, 33]. These manufacturing methods are too costly for today's global competition. The production of intermetallic compounds using these traditional methods requires expensive equipment and large amounts of energy. Thus, combustion synthesis is an advantageous method for

the production of these types of materials in many ways. Combustion synthesis of

intermetallic compounds does not require large amounts of energy, uses relatively simple

and inexpensive equipment, and has a much shorter processing time compared to that of

traditional manufacturing methods [2, 3]. Over the past twenty years, two classes of

alloying reactions have been the center of attention: nickel aluminides and titanium

aluminides. The current study focuses on combustion synthesis of the nickel aluminide

intermetallic compound Ni_3Al.

1.3 Introduction to Modeling and Simulation of Combustion Synthesis

Mathematical models of the combustion synthesis process have been developed to

supplement experimental efforts designed for characterizing intermetallic alloying

reactions. The most basic mathematical model of the SHS process was developed by

Novozhilov in [34] and was designed to model combustion of liquids and solids at the

continuum level. The model depicts the combustion wave propagating through the

intermetallic mixture. Equation (1.1) represents the temperature distribution of a two

dimensions system involving a single exothermic chemical reaction.

$$Cr\frac{\partial T}{\partial t} = \frac{\partial}{\partial x}\left(k\frac{\partial T}{\partial x}\right) + \frac{\partial}{\partial y}\left(k\frac{\partial T}{\partial y}\right) - Cru\frac{\partial T}{\partial x} + \Delta H_{RXN} rk_0 y(a) \cdot e^{\left(-E_a/RT\right)} \tag{1.1}$$

Equation (1.2) models the species distribution of the deficient reactant.

$$\frac{\partial a}{\partial t} = -u\frac{\partial a}{\partial x} - k_0 y(a) \cdot e^{\left(-E_a/RT\right)} \tag{1.2}$$

Here, x, is the primary coordinate that spans the length of the sample, y is the transverse

coordinate, t is time, T is the temperature, ? is the density, C is the heat capacity, and ? is

the thermal conductivity. ?H$_{RXN}$ represents the amount of energy liberated from the

alloying reaction, E_a is the activation energy of the reaction, k_0 is called the frequency factor, and R is the gas constant. The term ? (a) accounts for the reaction rate's dependence on the concentration of species a. The term u represents the velocity of propagation of the combustion wave. The solution of the system of equations is obtained through numerical methods where the equations are discritized using finite difference methods. Solutions to this system yield temperature profiles, species distribution profiles, and combustion wave velocities. Figure 1.1 shows an example of output obtained from this level of analysis.
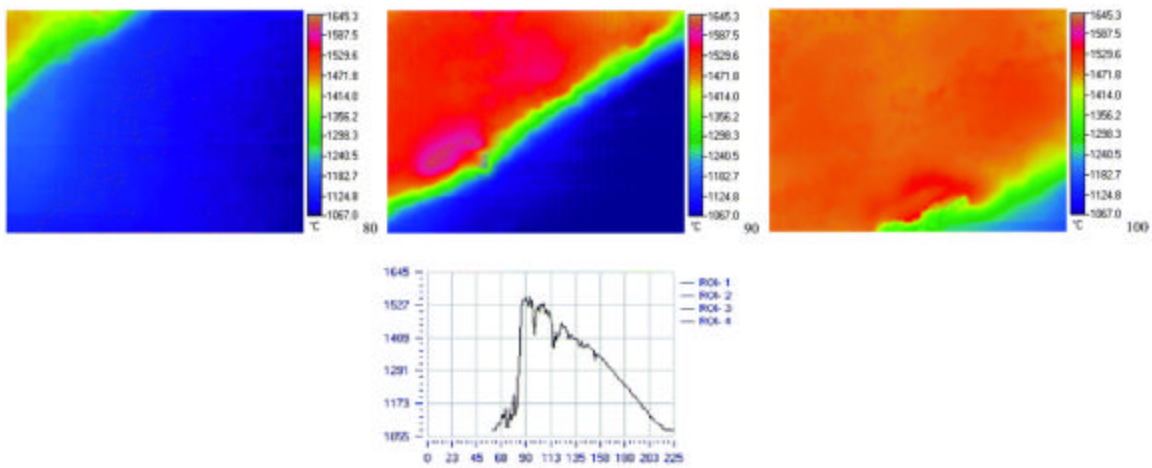
Figure 1.1 - Temperature contour snapshots of a combustion synthesis wave propagating through a sample (top). Temperature-time history of a point in the domain (bottom) [34].

The model given above is extensively used to analyze combustion synthesis at the continuum level. Although this type of analysis is extremely important in the design and production of intermetallic compounds, it is not the focus of the current research effort. This model can only be applied to systems whose alloying chemical reactions and material properties are well characterized. In many cases a system's chemical and

material properties are difficult, if not impossible to obtain through experiment. Often, the fidelity of the mathematical model used to describe the combustion synthesis of these systems strongly depends on results obtained from molecular scale modeling.

Molecular scale modeling, such as molecular dynamics simulation methods, can be used to obtain system properties that are used as inputs to continuum level models. Molecular dynamics simulations are often used to fully characterize reaction mechanisms of chemical systems. Thus, reaction rates and species concentrations can be determined. Additionally, molecular dynamics simulation methods provide a pathway to ascertain material properties of exotic intermetallic compounds that are not well characterized. Material and chemical properties that are commonly obtained from molecular dynamics simulation methods include density, heat capacity, coefficient of thermal expansion, mass diffusion coefficient, thermal diffusion coefficient, coefficient of thermal conductivity, heat of reaction, and activation energy.

Part of the current research effort is to develop a molecular dynamics simulation model that simulates shock wave induced combustion synthesis of intermetallic compounds such as Ni_3Al. The purpose of the model is to produce chemical and material properties of the alloying reactions. A major objective in developing the model is to design the simulation such that a relatively inexpensive experiment could be constructed to verify it. This is where existing molecular dynamics models fail. Most molecular dynamics models designed to simulate shock wave response of materials accurately capture the physics of the shock wave phenomenon, but fall short of accurately modeling the long-time diffusion controlled mechanism. These models are severely restricted to small simulation times that are governed by the shock wave velocity and system length.

In most cases the failure to capture the long time diffusion phenomenon is due to the treatment of the boundary conditions. Models generated to simulate long-time scale phenomena caused by shock wave loading are able to accurately simulate the state of the system after the attenuation of the shock wave, but the initial loading is modeled non-physically. These molecular dynamics models and there shortcomings are briefly described in [17], where an alternative model that captures short-time scale shock loading and long-time scale phenomenon is proposed. The proposed model simulates the initial shock loading by colliding two adjacent slabs of material together. Each slab of material is comprised of laminated (alternating) metallic layers. The collision results in the generation of two shock waves propagating in opposite directions from the center (collision point). When the shock waves reach the outer boundaries, (up to this point the spatial boundaries are modeled with shrink-wrapped boundary conditions and the transverse boundaries are modeled with periodic boundary conditions) the shrinking boundary conditions are replaced with periodic boundary conditions. Thus, at the end of the equilibrium molecular dynamics simulation, the entire system is in a shocked state and there is minimal translational motion. The equilibrium molecular dynamics simulation is carried out using a constant number of particles, volume, and energy (NVE) process.

Although this innovative model is able to simulate short-time and long-time phenomenon of a shock loaded sample, it possess a fundamental physical flaw. The problem arises from the application of periodic boundary conditions in the spatial coordinate during the equilibrium phase of the simulation. The accuracy of the shock wave physics that govern the series of complex reflected shock and relief waves,

generated by the shock impedance mismatch, is compromised. Also, an experiment that closely resembles this model would be extremely difficult and expensive to execute with success. The model that is developed in the current research effort uses a unique and innovative methodology to accurately capture the short-time and long-time physical and chemical phenomenon associated with the combustion of intermetallic systems.

1.4 The Ni/Al System

The Ni/Al system is comprised of several intermetallic compounds ranging from Al rich species such as Al_3Ni, Al_3Ni_2, and NiAl to Ni rich species such as Ni_3Al and Ni_5Al_3. The large majority of current research efforts have been focused on the NiAl and Ni_3Al species due to the enhanced mechanical properties. Figure 1.2 shows the phase diagram for the nickel aluminum system.
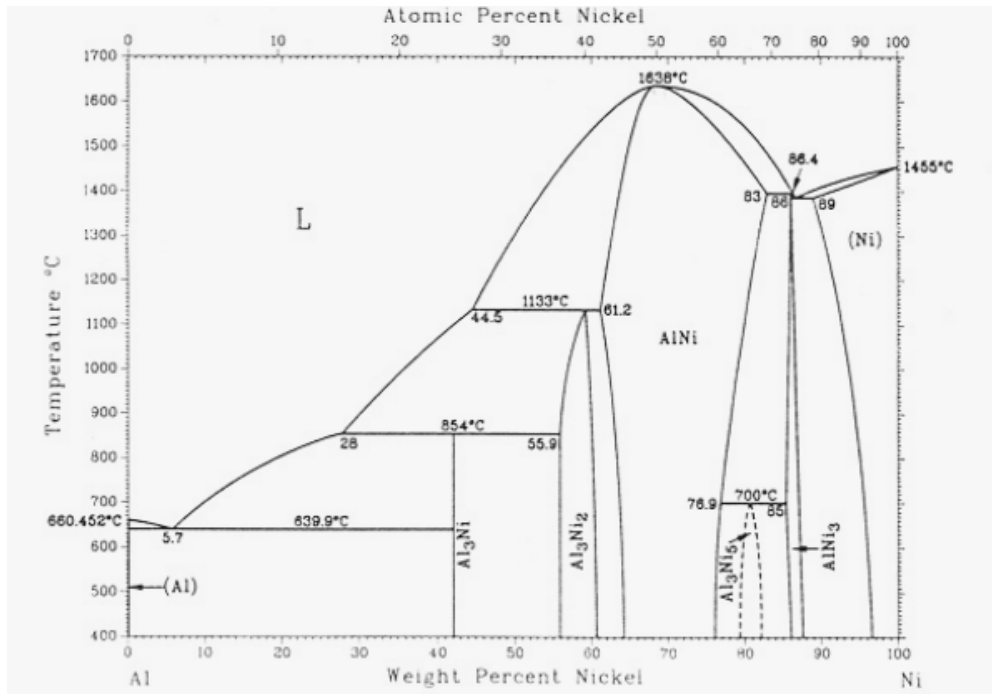
Figure 1.2 – The Ni/Al system phase diagram [35].

10

1.4.1 Enhanced Properties of Ni₃Al

The many beneficial characteristics of nickel aluminide compounds promote their use in modern, highly specialized machines. For most applications, the density is considered to be low and the raw material is relatively inexpensive. Ni₃Al based alloys show excellent resistance to oxidation at temperatures exceeding 900 °C, they have good high-temperature ductility for nickel-rich compositions, and they possess high-temperature strength up to temperatures approaching 1100 °C. They have good resistance to carburization and they show an increase in yield strength for temperatures around 850 °C [36]. Disadvantages of nickel aluminides include poor ductility and high propensity of fracture due to the brittle nature of the polycrystalline structure [37]. It is known that these shortcomings can be overcome through the use of additive dopants. It was shown that the ductility of Ni₃Al dramatically improved with the addition of small amounts boron [38].

1.4.2 Some Current Applications of the Ni₃Al Intermetallic Compound

Sikka and Deevi have compiled a detailed list of intermatallic compounds used in structural applications for general use [39]. The following applications and objectives are taken from their work. Ni₃Al based alloys are used for radiant burner tubes in heat-treating furnaces. Here, the application of Ni₃Al helps to increase the life of the furnace due to its higher creep, oxidation, and carburization resistance properties. Ni₃Al based alloys are also used extensively for die tools, especially dies that are designed for hot-forging processes and for hot pressing of permanent magnet materials. The life cycle of a Ni₃Al based die is increased mainly due to the peak in yield strength that exists at 850 °C and good oxidation resistance. Ni₃Al powder is used as a binder for tungsten and

chromium carbide tools and dies. In this application, Ni_3Al improves hardness, wear

resistance, and aqueous corrosion resistance in certain acid solutions.

1.4.3 Self-Propagating High-Temperature Combustion Synthesis of Ni_3Al

In general, nickel aluminide reactions are of interest for various applications. The

current study concentrates on the formation of the Ni_3Al nickel aluminide compound.

Experimental efforts using the SHS method of combustion synthesis for characterizing

the Ni_3Al nickel aluminide system have been carried out with some success. Varma and

Mukasyan reported that the adiabatic combustion temperature of the reaction is 1586 K

and that the maximum measured combustion temperature was 1690 K [40]. Table 1.1

shows simple combustion properties of Ni/Al systems.

Table 1.1 - Combustion properties of nickel aluminide systems [40].

System	Adiabatic temperature (K)	Product melting point (K)	Combustion velocity (cm/s)	Combustion regime
Ni + 3Al	1396	1127	0.09	Strong pulsating
2Ni + 3Al	1867	1405	0.93	Weak pulsating
Ni + Al	1911	1911	1.24	Steady state
3Ni + Al	1586	1753	0.22	Pulsating

It is interesting to note that the combustion temperature of Ni_3Al is higher than the

melting point of aluminum and the aluminum-rich intermediate species of the reaction,

lower than the melting point of nickel, and roughly equivalent to the melting point of the

product species. The physical mechanism describing the reaction $3Ni + Al \rightarrow Ni_3Al$ is

still somewhat unknown. Varma and Mukasyan offer a fairly good description of the

SHS diffusion controlled reaction based on experimental findings.

"Aluminum melts and rapidly spreads around the Ni particles, with simultaneous

formation of Al-rich phases (Ni_2Al_3 and probably even $NiAl_3$). The diffusion of metals

through the layer of the intermediate product appears to be the limiting stage of the combustion process. A study of reactions in the Ni-Al system showed that diffusion in this case occurs mainly due to migration of Ni in molten Al [41]. *Thus the reaction proceeds by the diffusion of Ni through intermediate layer (NiAl₃ and Ni₂Al₃), whose thickness remains essentially constant during the reaction* [42]. *The final product (Ni₃Al) crystallizes in the volume of the melt after saturation."*

Using this model, researchers have been able to develop a kinetic expression for the diffusion-controlled rate and an analytical expression for the combustion wave velocity [43, 44]. These observations describe, in a general way, a basic mechanism for how the $3Ni + Al \rightarrow Ni_3Al$ reaction progresses through time. However, they are qualitative, unproven, and largely incomplete. Much work is needed to validate and verify these results. Also, quantitative research efforts would give much needed insight into the entire chemical reaction mechanism (e.g. the rate formation and deformation of intermediate species as well as the formation of product species). Philpot, Munir, and Holt made an attempt at characterizing the chemical reaction mechanism for volume combustion synthesis (VCS) methods (relatively slow heating rates) [45]. They proposed the following mechanism:

(1) The following solid-solid reaction initiates the mechanism:

$$3Al + Ni \rightarrow NiAl3 \qquad\qquad -?H = 260cal/g$$

(2) Formations of other Al-rich species occur through the following intermediate reactions:

$$3Al + Ni \rightarrow Ni_2Al_3 \qquad\qquad -?H = 324cal/g$$

$$Al_3Ni + Ni \rightarrow Ni_2Al_3 \qquad\qquad -?H = 324cal/g$$

13
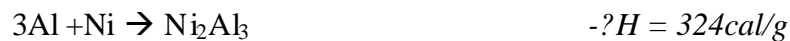
(3) Traces of NiAl and Ni_3Al species appear by weak exothermic reactions between Ni

and Al-rich species.

$$Ni_2Al_3 + 7Ni \rightarrow 3Ni_3Al \qquad\qquad \textit{-?H ~ 0cal/g}$$

$$Ni_2Al_3 + Ni \rightarrow 3NiAl \qquad\qquad \textit{-?H ~ 0cal/g}$$

(4) The solid-liquid reaction of Al-rich and Ni

$$Ni + Ni_xAl_y \rightarrow Ni_3Al$$

Experimental efforts have shown that the enthalpy of reaction is [46, 47]:

$$3Ni + Al \rightarrow Ni_3Al \qquad\qquad \textit{-?H = 192.91cal/g}$$

Further experimental efforts are required to test and prove proposed reaction mechanisms

such as this. Often, experiments are costly and have a limited range of visibility for

obtaining the desired measurements. Modeling and simulation can observe what is

undetectable to experiment. Thus, modeling and simulation gives much needed insight

into the inner workings of the chemical reaction.

CHAPTER 2

INTRODUCTION TO MOLECULAR DYNAMCIS SIMULATION METHODS

2.0 Introduction

Molecular dynamics methods serve as instruments for modeling and predicting material response to some external stimulus, often mechanical in nature. Material responses are characterized by observing consecutive particle arrangements and particle interactions in time. Each arrangement is obtained by integrating Newton's laws of motion that describe the previous arrangement. The end result is a list of particle trajectories that illustrate the motion of the system. A particle's trajectory can be thought of as a reaction or a series of reactions due to an initial action or stimulus. A system's reaction to an initial action is characterized by changes in mechanical and thermodynamic properties. Properties are calculated from the particle trajectories through the use of kinetic theory, statistical thermodynamics, and sampling theory. Static system property functions, such as temperature, internal energy, and pressure, are calculated from averages of either the Hamiltonian or it's spatial and momentum derivatives. Dynamic system properties, such as viscosity, thermal conductivity, and diffusion coefficients, are calculated through the use of time correlation functions [48].

2.1 Fundamental Equations of Motion

2.1.1 Newton's Equations of Motion

The fundamental governing equations used in molecular dynamics are Newton's equations of motion. Newton's three laws of motion for a multibody system are stated as follows [49]:

1. **An object at rest remains at rest and an object in motion will continue in motion with a constant velocity (that is, constant speed in a straight line) unless it experiences a net external force.**

$$\frac{d\vec{r}_i}{dt} = Const \tag{2.1}$$

where $\vec{r}_i$ is the vector that determines the ith atom's or molecule's location relative to the

origin of the Eulerian (fixed) coordinate system.

2. **The acceleration of an object is directly proportional to the net force acting on it and inversely proportional to its mass.**

$$\vec{F}_i = m_i \frac{d^2 \vec{r}_i}{dt^2} \tag{2.2}$$

where m_i is the mass and $\vec{F}_i$ is the net external force acting on the ith atom or molecule.

3. **If two bodies interact, the force exerted on body 1 by body 2 is equal to and opposite the force exerted on body 2 by body 1.**

$$\vec{F}_1 = -\vec{F}_2 \tag{2.3}$$

In classical dynamics, a particle's kinetic energy is defined as the work required to move

the particle from rest to velocity $\dfrac{d\vec{r}_i}{dt}$.

$$E_{k_i} = \frac{1}{2} m_i \cdot \left[\frac{d\vec{r}_i}{dt} \right]^2 \tag{2.4}$$

2.1.2 Hamilton's Equations of Motion

The Hamiltonian $\tilde{H}$ is a function of the particles' positions and velocities whose

value is constant with respect to time.

$$\tilde{H}\left(\vec{r}^N, \vec{p}^N\right) = Const \tag{2.5}$$

16

The notation $\vec{r}^N = \{\vec{r}^1, \vec{r}^2, \vec{r}^3, ..., \vec{r}^N\}$ is the set of vectors that locate the atomic centers of

mass. $\vec{p}^N = \{\vec{p}^1, \vec{p}^2, \vec{p}^3, ..., \vec{p}^N\}$ is the set of vectors that lists the momentum of each

atom. Here, momentum for an individual atom or molecule is defined as:

$$\vec{p} = m \cdot \frac{d\vec{r}}{dt} \tag{2.6}$$

For isolated systems, the Hamiltonian is recognized as the total energy of the system.

The total energy of an isolated system is defined as the sum of the kinetic and potential

energies of each atom.

$$E_T = H(\vec{r}^N, \vec{p}^N) = \sum_i \frac{\vec{p}_i^2}{2m_i} + U_{P.E.}(\vec{r}^N) \tag{2.7}$$

where the potential energy $U_{P.E.}$ is defined for particle interactions. The equations of

motion are obtained from the total time derivative of the Hamiltonian.

$$\frac{dH}{dt} = \sum_i \frac{\partial H}{\partial \vec{p}_i} \cdot \frac{d\vec{p}_i}{dt} + \sum_i \frac{\partial H}{\partial \vec{r}_i} \cdot \frac{d\vec{r}_i}{dt} + \frac{\partial H}{\partial t} \tag{2.8}$$

Note that the Hamiltonian is constant with respect to time and has no explicit time

dependence. So, the general expression becomes:

$$\sum_i \frac{\partial H}{\partial \vec{p}_i} \cdot \frac{d\vec{p}_i}{dt} + \sum_i \frac{\partial H}{\partial \vec{r}_i} \cdot \frac{d\vec{r}_i}{dt} = 0 \tag{2.9}$$

Taking the total time derivative of (2.7) for an isolated system yields:

$$\frac{dH}{dt} = \sum_i \frac{\vec{p}_i}{m_i} \cdot \frac{d\vec{p}_i}{dt} + \sum_i \frac{\partial U_{P.E.}}{\partial \vec{r}_i} \cdot \frac{d\vec{r}_i}{dt} = 0 \tag{2.10}$$

Comparing (2.9) with (2.10) and using the definition of momentum given by (2.6), it is

observed that

$$\frac{\partial H}{\partial \vec{p}_i} = \frac{\vec{p}_i}{m_i} = \frac{d\vec{r}_i}{dt} \tag{2.11}$$

17

$$\frac{\partial H}{\partial \vec{r}_i} = \frac{\partial U_{P.E.}}{\partial \vec{r}_i} \tag{2.12}$$

Substituting (2.11) into (2.9) yields

$$\frac{dH}{dt} = \sum_i \frac{d\vec{r}_i}{dt} \cdot \frac{d\vec{p}_i}{dt} + \sum_i \frac{\partial H}{\partial \vec{r}_i} \cdot \frac{d\vec{r}_i}{dt} = 0 \tag{2.13}$$

$$\sum_i \left(\frac{d\vec{p}_i}{dt} + \frac{\partial H}{\partial \vec{r}_i} \right) \left(\frac{d\vec{r}_i}{dt} \right) = 0 \tag{2.14}$$

Due to the fact that all the velocities are independent from one another and the result

(2.12), (2.14) is satisfied only if, for each molecule i

$$\frac{\partial U_{P.E.}}{\partial \vec{r}_i} = -\frac{d\vec{p}_i}{dt} \tag{2.15}$$

Using (2.15), (2.6), and Newton's second law, the following conclusion of obtained:

$$\vec{F}_i = -\frac{\partial U_{P.E.}}{\partial \vec{r}_i} \tag{2.16}$$

Equations (2.11) and (2.15) are known as Hamilton's equations of motion and represent

six equations for each atom. They are first order in nature; where as Newton's three

equations of motion are second order in nature. Result (2.16) is an important relation that

is the main driving force behind molecular dynamics. The derivation of Hamilton's

equations of motion is taken from Haile [48].

2.2 Modeling Molecular Interactions

In molecular dynamics, molecular interactions must be accounted for.

Interactions between molecules or atoms are described by intermolecular potentials

which define the potential energy between molecules or atoms as a function of the

separation distance. The strong majority of intermolecular potentials are pairwise

additive or at least include a pairwise additive term. It is assumed that in pairwise

additive potentials that the interaction energy among n atoms is the sum of each two-

body contribution. There are two fundamentally different types of models used for

simulating particle interactions; those for hard spheres, for which the potential energy

between two particles is discontinuous, and those for soft spheres, for which the potential

energy between two particles is a continuous function of separation distance.

2.2.1 Hard Sphere Model

In the hard sphere model for simulating molecular interactions, the pairwise

potential energy function is a delta function.

$$U_{P.E.}(r) = \begin{cases} \infty & r \leq h \\ 0 & r > h \end{cases} \tag{2.17}$$

A plot of the delta function representing the intermolecular potential versus separation

distance is shown in Figure 2.1. The plot shows that there are no interactions between the

atoms except when they collide.
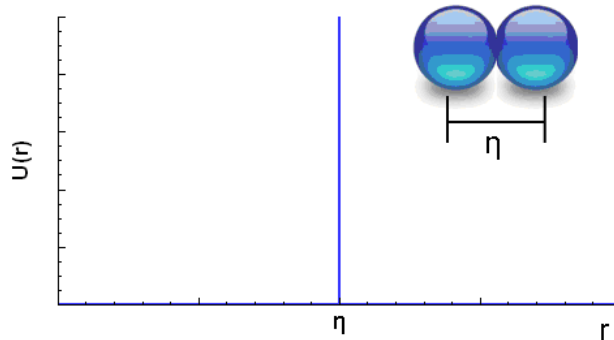
Figure 2.1 – The pair potential energy function for the hard sphere model.

Collisions of the atoms or particles are taken to be perfectly elastic. The particles behave

like colliding billiard balls. No particle deformation is experienced during collisions.

19

Also, the internal state of the particles remains constant. The kinematic equations that govern the motion of hard sphere interactions are derived from the conservation of linear momentum and the conservation of energy.

$$\sum_i m_i v_{i_0} = \sum_i m_i v_{i_f} \tag{2.18}$$

$$\sum_i \frac{1}{2} m_i v_{i_0}^2 = \sum_i \frac{1}{2} m_i v_{i_f}^2 \tag{2.19}$$

Here, the equations of motion are nothing more than algebraic equations. Unlike Newton's equations of motion, these equations can be easily solved without numerically solving differential equations. Another advantage of the hard sphere model is that particle interactions range over relatively short distances. Short distance interactions reduce the computational time by a significant amount. Results generated from the hard sphere model are reasonably consistent with other simulation methods such as Monte Carlo simulations [50]. Although the hard sphere model presents several advantages and short cuts, there are many severe drawbacks to using it. It is extremely difficult to accurately simulate phase transitions for most models that use the hard sphere method. Simulations that use the hard sphere model exhibit a high level of dependence on number of atoms. Also, there are several computational difficulties associated with the model when used to simulate complex systems. Assessing statistical and systematic errors as well as detecting system equilibrium can be very arduous.

Given the availability of computational resources with modern computer systems and the advancements made in the field over the past thirty years, the hard sphere model for simulating molecular interactions serves more as a learning tool rather than an actual method that is used in current molecular dynamics simulations.

2.2.2 Soft Sphere Models

In soft sphere models for simulating molecular interactions, the pairwise additive potential energy function is of the form

$$U_{P.E.}\left(\vec{r}^{N}\right) = \sum_{I<J}\sum U_{P.E.}\left(r_{ij}\right) \tag{2.20}$$

where r_{ij} is the scalar distance between the centers of atom i and atom j. Here, instantaneous multiple body interactions are ignored. The functional form of $U_{P.E.}(r_{ij})$ is continuous and differentiable for all values of $r_{ij} > 0$. Given this form, it is clear why result (2.16) is critical to molecular dynamics simulation methods. It relates molecular interactions to Newton's second equation of motion.

$$\vec{F}_i = -\frac{\partial U_{P.E.}}{\partial \vec{r}_i} \tag{2.21}$$

The Lennard-Jones (12, 6) potential energy model is commonly used to demonstrate qualitative aspects of soft sphere potentials [51].

$$U_{P.E.}(r) = 4e\left[\left(\frac{s}{r}\right)^{12} - \left(\frac{s}{r}\right)^{6}\right] \tag{2.22}$$

where s is the distance to the bottom of the energy well and e is the energy well depth. These parameters can be obtained by curve fitting experimental data or by quantum chemistry simulation results. The resulting intermolecular force is

$$F(r) = \frac{dU_{P.E.}(r)}{dr} = 24\frac{e}{s}\left[2\left(\frac{s}{r}\right)^{13} - \left(\frac{s}{r}\right)^{7}\right] \tag{2.23}$$

Here, the convention is that attractive forces are negative and repulsive forces are positive. The Lennard-Jones model, as well as most soft sphere models, captures short-range, repulsive forces as well as long-range attractive forces. Repulsive forces occur as

21

a result of overlapping of the atoms' electron clouds; this is known as Pauli's repulsion. The attractive forces are a consequence of London dispersion interactions.
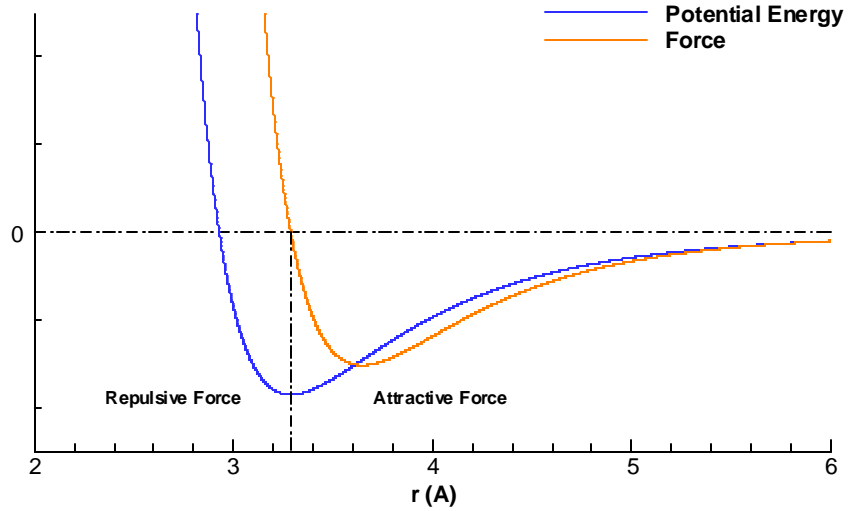
Figure 2.2 – The Lennard-Jones (12, 6) pair potential and pair force representing interactions between hydrogen atoms.

For systems containing a large number of atoms, the number of unique pair interactions is rather sizeable and can severely increase the computation time. For a system containing n atoms, the number of unique pair interactions is

$$\frac{1}{2} n \cdot (n-1) = \frac{n^2}{2} - \frac{n}{2}$$

(2.24)

Hence, the number of interactions increases with the square of the number of atoms. In order to deal with this problem, many potential functions include a cutoff distance where pair interactions beyond this distance are neglected.

$$U_{P.E.}(r) = \begin{cases} 4\boldsymbol{e}\left[\left(\dfrac{\boldsymbol{s}}{r}\right)^{12} - \left(\dfrac{\boldsymbol{s}}{r}\right)^{6}\right] & r \leq r_c \\ 0 & r > r_c \end{cases}$$

(2.25)

This method of modeling molecular interactions can significantly reduce the computational expense and can make a simulation feasible that, without it, was impractical. Figure 2.2 shows that the force acting between two hydrogen atoms becomes negligible at relatively short separation distances. Thus, this approximation is valid for many potentials and systems.

Due to its simple form, the Lennard-Jones (12, 6) potential function serves as an excellent qualitative learning tool. Many other types of intermolecular potential functions that are used in molecular dynamics simulations are more robust than the Lennard-Jones potential function. A few other potentials that are commonly used in molecular dynamics simulations are the Buckingham potential, Embedded Atom Method potential, and the Morse potential. Each potential function has its strengths and weaknesses and some potential functions are specifically designed to model exact physical phenomenon. For example, the Embedded Atom Method is explicitly designed to model metals and metal alloys and the Buckingham potential is used to model Coulombic interactions.

Using soft sphere models to simulate molecular interactions has tremendous advantages over the hard sphere model. Currently, almost all molecular dynamics simulations are executed using some type of soft sphere intermolecular potential function. The functional form of soft sphere models enables the forces acting on each atom to be readily calculated and substituted into Newton's second law so that the atom accelerations can be determined.

2.3 Computational Algorithm

Typically, in molecular dynamics simulations, Newton's equations of motion are numerically solved using a finite-difference method known as Verlet's algorithm. The algorithm is a third-order Störmer algorithm and was proposed by the French physicist Loup Verlet in 1967 [52]. The algorithm is comprised of two Taylor series expansions that represent the atom's position. The first series expansion marches forward in time.

$$x(t + \Delta t) = x(t) + \frac{dx(t)}{dt}\Delta t + \frac{1}{2}\frac{d^2x(t)}{dt^2}\Delta t^2 + \frac{1}{3!}\frac{d^3x(t)}{dt^3}\Delta t^3 + O(\Delta t^4) \qquad (2.26)$$

The second series expansion marches backward in time.

$$x(t - \Delta t) = x(t) - \frac{dx(t)}{dt}\Delta t + \frac{1}{2}\frac{d^2x(t)}{dt^2}\Delta t^2 - \frac{1}{3!}\frac{d^3x(t)}{dt^3}\Delta t^3 + O(\Delta t^4) \qquad (2.27)$$

The odd-ordered terms are eliminated when the two series expansions are added together.

$$x(t + \Delta t) = 2x(t) - x(t - \Delta t) + \frac{d^2x(t)}{dt^2}\Delta t^2 + O(\Delta t^4) \qquad (2.28)$$

This very simple, yet powerful result is Verlet's algorithm for atom positions. The term on the left hand side of the equation represents the next position of the atom. The first term on the right hand side of the equation is two times the current position of the atom. The second term corresponds to the previous position of the atom. The third term on the right hand side is the current acceleration of the atom times the square of the time step. Here, the acceleration is calculated from the intermolecular forces and Newton's second law. The equation has third order truncation error. Because the algorithm calculates the next position based on the current and previous positions, an additional equation is needed to solve for the previous position at time zero. This can be done by truncating (2.27) after the first-order term.

$$x(t - \Delta t) = x(t) - \frac{dx(t)}{dt} \Delta t \tag{2.29}$$

This is known as the backward time marching Euler method. It states that the previous atom position is equal to the current position minus the current velocity times the time step. It is only used in the first step to initiate the simulation.

Since (2.28) does not contain the velocity, a variety of schemes have been contrived to fill in this gap. The simplest being a first-order central difference estimator, which is obtained by further truncating (2.26) and (2.27) to get:

$$x(t + \Delta t) = x(t) + \frac{dx(t)}{dt} \Delta t + \frac{1}{2} \frac{d^2 x(t)}{dt^2} \Delta t^2 \tag{2.30}$$

$$x(t - \Delta t) = x(t) - \frac{dx(t)}{dt} \Delta t + \frac{1}{2} \frac{d^2 x(t)}{dt^2} \Delta t^2 \tag{2.31}$$

Subtracting (2.31) form (2.30) yields:

$$\frac{dx(t)}{dt} = \frac{x(t + \Delta t) - x(t - \Delta t)}{2\Delta t} \tag{2.32}$$

Accuracy of the velocity is critical in determining system properties. Both the system kinetic energy and temperature depend highly on atom velocities. Therefore, it is vital to use an algorithm that is of high fidelity. The algorithms shown in this section form the basic foundation of most integration methods used in molecular dynamics simulations. More robust versions of Verlet's algorithm have been developed that are currently in use. This section is only meant to serve as an introduction to integration in molecular dynamics simulations.

2.4 Timestep and Algorithm Stability

The timestep in numerical methods used to solve differential equations is often determined from rigorous stability analysis. Von Neumann developed a seemingly elegant way of performing stability analysis for finite difference equations of partial differential equations. Unfortunately, most finite difference equations used in molecular dynamics are nonlinear. The following example demonstrates this point. Consider the two-body, one-dimensional system shown in Figure 2.3.
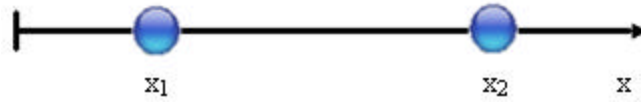
Figure 2.3 – A two-body, one-dimensional system that is modeled using the Lennard-Jones (12, 6) potential and Verlet's algorithm.

Using Verlet's algorithm and the Lennard-Jones (12, 6) potential function, the governing finite difference equation is obtained as:

$$x_1(t + \Delta t) = 2x_1(t) - x_1(t - \Delta t) - \frac{4e}{m}\left[\left(\frac{12s^{12}}{(x_2(t) - x_1(t))^{13}}\right) - \left(\frac{6s^6}{(x_2(t) - x_1(t))^7}\right)\right]\Delta t^2 \qquad (2.33)$$

The nonlinearities in (2.33) stem from the Lennard-Jones (12, 6) potential. Thus, the analytic stability analysis described by von Neumann's method does not apply. However, for general nonlinear equations, approximate stability analysis can be performed by linearizing the equation or using the methods of Lyapunov [53]. Unfortunately, both of these methods are not a viable option when applied to the equations of motion used in molecular dynamics. Therefore, there is no simple analytical way to obtain an appropriate value for a timestep. Typically, the timestep is determined though performing a series of trial simulations.

2.5 Boundary Conditions

The objective of most molecular dynamics simulations is to obtain bulk properties that are representative of macroscopic phenomena. In atomistic simulations, boundary effects influence a significant portion of the system which can cause the system properties to resemble surface phenomena rather than bulk phenomena. A simple example that Leach gives illustrates this point [54].

"Suppose we have a cube of volume 1 liter which is filled with water at room temperature. The cube contains approximately 3.3×10^{25} molecules. Interactions with the walls can extend up to 10 molecular diameters into the fluid. The diameter of the water molecule is approximately 2.8 Å and so the number of water molecules that are interacting with the boundary is about 2.0×10^{19}. So, only about one in 1.5 million water molecules is influenced by interactions with the walls of the container. The number of particles in a Monte Carlo or molecular dynamics simulation is far fewer than 10^{25} – 10^{26} and is frequently less than 1000. In a system of 1000 water molecules most, if not all of them, would be within the influence of the walls of the boundary. Clearly, a simulation of 1000 water molecules in a vessel would not be an appropriate way to derive bulk properties. The alternative is to dispense with the container altogether. Now, approximately three-quarters of the molecules would be at the surface of the sample rather than being in the bulk. Such a situation would be relevant to studies of liquid drops, but not to studies of bulk phenomena".

Thus, appropriate boundary conditions are essential to modeling atomistic behavior. There is a wide variety of boundary conditions used in molecular dynamics

simulations. The more commonly used boundaries are periodic, fixed, shrink wrapped, and perfectly/partially reflective.

2.5.1 Periodic Boundary Conditions

Periodic boundary conditions make it possible for a small collection of atoms to be representative of bulk material. The schematic shown in Figure 2.4 illustrates that atoms contained within a small volume experience forces similar to those found in bulk material. The entire system volume is comprised of a primary cell, located in the center, surrounded by exact replicas of itself. The replica cells, also known as image cells, contain the exact number of atoms as the primary cell. Also, atoms within the image cells have the same position and momentum as the corresponding atoms within the primary cell. When a particle translates outside of the primary cell, it is replaced by a particle from an adjacent image cell that enters from the opposite side. Hence, the number of particles remains constant throughout the simulation.
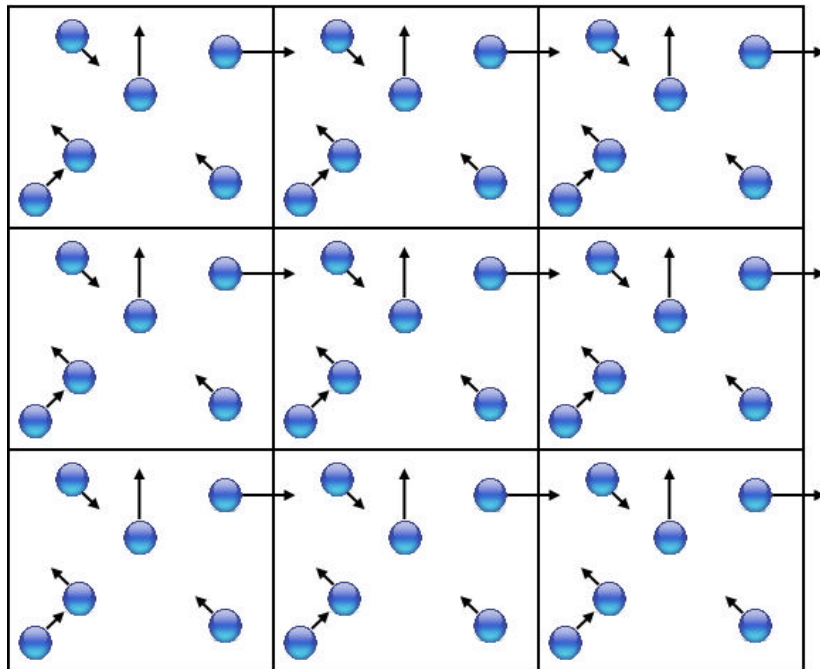
Figure 2.4 – Periodic boundary conditions in two dimensions.

When periodic boundary conditions are used, an atom located inside the primary cell has molecular interactions with atoms inside image cells as well as atoms inside the primary cell. As a result, surface effects are eliminated from the primary cell.

2.5.2 Fixed Boundary Conditions

The fixed boundary condition is non-periodic, so that particles do not interact across the boundary. Also, they do not move from one side of the cell to the other. In three dimensions, the boundary is represented by a planer surface. If an atom moves across the planer surface boundary, then it is lost to the system. Consequently, the mass is not conserved throughout the length of the simulation.
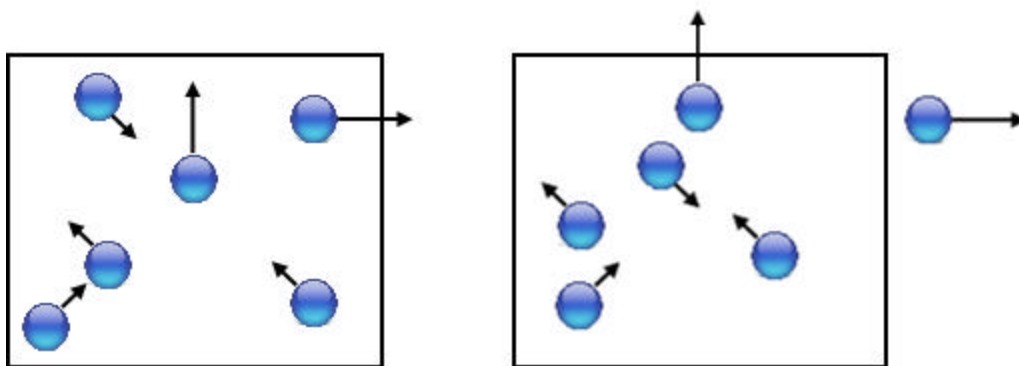
Figure 2.5 – Snapshots of a system using fixed boundary conditions; once the atom leaves the boundary, it is no longer part of the simulation.

2.5.3 Shrink Wrapped Boundary Conditions

The Shrink Wrapped boundary condition is also non-periodic, so that particles do not interact across the boundary and do not move from one side of the cell to the other. In three dimensions, the boundary is represented by a planer surface. If an atom moves across the planer surface boundary, then the planer surface is translated such that the

atom is still contained within the system. Unlike the system with fixed boundary

conditions, the mass is conserved throughout the length of the simulation.
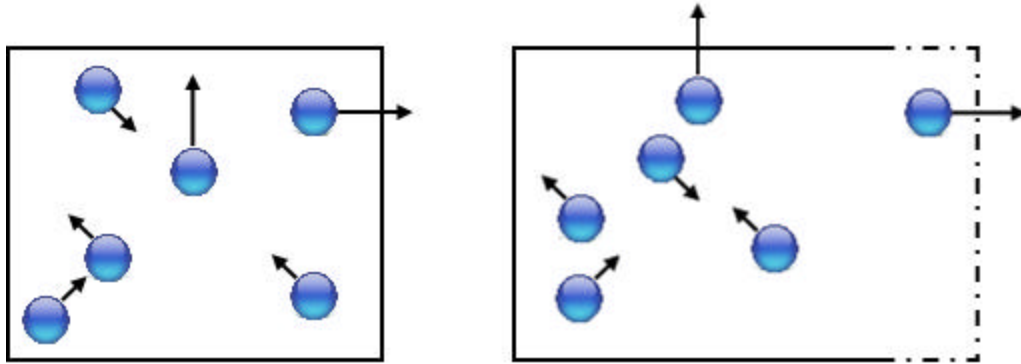
Figure 2.6 – Snapshots of a system using shrink wrapped boundary conditions; when the atom leaves the boundary, the boundary is extended.

2.5.4 Perfectly/Partially Reflective Boundary Conditions

Perfectly reflective boundary conditions are also non-periodic, so that particles do

not interact across the boundary and do not move from one side of the cell to the other.

They bound the initial simulation domain with one or more walls which reflect particles

when they attempt to move thru them. Here, reflection is defined as follows: when an

atom translates thru the fixed boundary on a time-step by some distance ? X, it is

perfectly reflected about the fixed boundary back inside the domain and the velocity

component, perpendicular to the boundary, is flipped. This is illustrated in Figure 2.7.
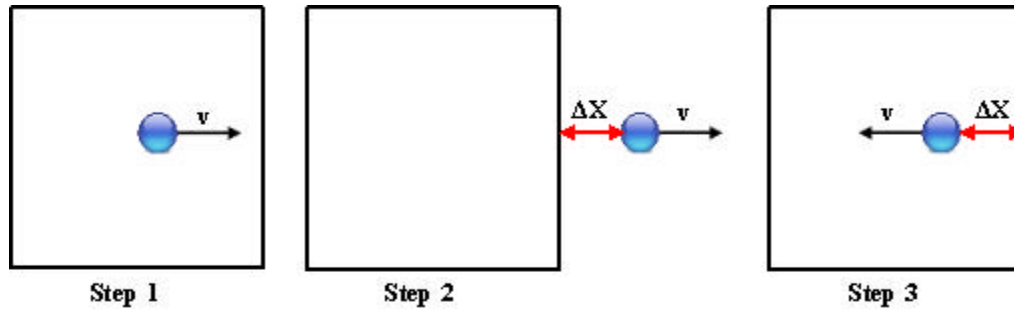
Figure 2.7 – An illustration of perfectly reflective boundary conditions. Step 1 shows the atom just before leaving the boundary. Step 2 shows the atom outside the boundary by a distance ?X with velocity V in the positive direction. Step 3 shows the atom is place back inside the boundary by a distance ?X with a velocity ? in the negative direction.

In addition to perfectly reflecting boundary conditions, there are partially reflecting boundary conditions. Essentially, they act in the same manner as the perfectly reflecting boundary condition with the exception that the magnitudes of the displacement and velocity are reduced by some fraction when placed back inside the domain. Note that these boundaries are not used with constant volume, energy, and number of particles (NVE) simulations due to the energy loss associated with a partial reflection.

2.6 Initial Conditions

Assigning initial conditions to the system entails assigning initial atom positions, initial atom velocities, and possibly, initial values for higher derivatives of the atom positions. Initial positions are not assigned in a random fashion due to the artificially large amount of overlap that occurs between two neighboring atoms. Instead, initial positions are often assigned in accordance with a lattice structure or are taken from a previous simulation. Initial velocities are randomly assigned using a random number generator with the specified seed as the specified temperature. Often, the initial

velocities are randomly assigned in a Gaussian distribution. They can also be assigned by reading in a file from a previous simulation.

2.7 Equilibration and Production

After initialization of the simulation is completed, the numerical algorithm can begin computing the system of equations. Molecular dynamics simulations are broken up into two phases. The first phase, called equilibration, relaxes the system from somewhat arbitrarily assigned initial positions and velocities to an equilibrium state. Adjustments to the system temperature by rescaling the velocities are typically performed in this phase of the simulation. For example, a simulation of solid aluminum may begin at 0 K where each atom is located at a crystal lattice sight. During the equilibration phase of the simulation, the aluminum lattice may be heated to 300 K (room temperature) by rescaling the atom velocities at a prescribed interval. The end result is that the aluminum has reached an equilibrium state with a temperature of 300 K. During the equilibration phase of the simulation, property averages are unstable, especially if velocity rescaling is used. Although the system properties of the equilibration phase are not used for calculating bulk material properties, they are used to monitor the system and to identify when the system reaches equilibrium. Haile lists five necessary conditions that an isolated system at an equilibrium state should satisfy [48].

1. The total number of molecules n and total energy E_T should be constants, independent of time. Since E_T is constant, fluctuations in the kinetic energy and potential energy must be equal in magnitude but out of phase with one another.

2. Each Cartesian component of the velocities should, on a time average, describe a Maxwell distribution. If velocity rescaling is performed with a Gaussian distribution, then the velocities are ensured to have a Maxwell distribution.

3. Thermodynamic properties, such as the temperature, configurational internal energy, and pressure, should be fluctuating about table average values. These averages should be independent of how the equilibrium state was attained. Thus, at a specified state condition, averages should be reproduced when a run is repeated from different assignments of initial positions and initial velocities. The magnitudes of the fluctuations depend on the system size, that is, on the number of atoms n; in particular, the fluctuations decrease as $n^{1/2}$. Thus, when we increase the number of atoms from 108 to 500, the magnitude of fluctuations are roughly halved.

4. Property averages should be stable to small perturbations. If the state is disturbed, for example by momentarily adding then removing a small amount of heat, thermodynamic properties should recover their equilibrium values. Such small perturbations often can disrupt metastable states, which otherwise may exhibit some features of equilibrium.

5. If the system is divided into macroscopic parts, time averages for each property should be the same in each part. For example, imagine that we arbitrarily divide the system in half. When averaged over a finite duration, the number of molecules, temperature, total energy, and pressure in the two halves should each be the same.

Once equilibrium is reached, the production phase of the simulation can begin. Nothing

about the algorithm has changed; the only difference is that system properties are used to

calculated material characteristics. Note that in current molecular dynamics simulations

it is common practice to change boundary conditions at this point in the simulation.

2.8 Calculating Basic System Properties

The goal of many molecular dynamics simulations is to characterize a substance

or material by calculating macroscopic system properties from molecular interactions.

Calculating system properties from a simulation of molecules or atoms involves analysis

of trajectories. The output of the simulation is a file containing the phase-space

trajectories (time, position, and velocity) of all the atoms. From the phase-space

trajectories, all thermodynamic and static structure quantities can be calculated.

Molecular theory of matter states that macroscopic properties are a consequence

of molecular interactions. Furthermore, for an isolated system with a fixed volume at

thermodynamic equilibrium, any measurable macroscopic property can be represented by

a mathematical function that depends only on the phase-space trajectories of the system

atoms. Thus, over the time period from t_0 to $t_0 + t$, the measurable property is represented

by the expression:

$$A_{Measured} = \frac{1}{t} \int_{t_0}^{t_0+t} A\left(\vec{r}^N(t), \vec{p}^N(t)\right) dt \qquad (2.34)$$

It is assumed that at thermodynamic equilibrium the measurable property, which is

averaged over the period t_0 to $t_0 + t$, is representative of the average property over an

infinite time period.

$$\langle A \rangle = A_{Measured} \tag{2.35}$$

$$\langle A \rangle = \underset{t \to \infty}{Lim} \frac{1}{t} \int_{t_0}^{t_0+t} A\left(\vec{r}^N(t), \vec{p}^N(t)\right) dt \tag{2.36}$$

Here, the equations used to calculate basic thermodynamic properties from simulation phase-space trajectories are shown. Many more property functions are defined and are available but are beyond the scope of the current work and will therefore not be considered here.

The internal energy of an isolated system is comprised of two components; the kinetic (sensible) energy and the potential (configurational) energy. In thermodynamics, the kinetic energy contribution to the internal energy encompasses molecular translation, rotation, and vibration, as well as electron translation, electron spin, and nuclear spin. In classical molecular dynamics, atoms have spherical symmetry defined by an average radius. The potential energy function describes all the internal characteristics of the molecule (atom). That is to say, the potential function accounts for the interactions of the electrons and protons as well as other coulumbic interactions (van der Waals forces) using a single potential energy surface. This is a consequence of the Born-Oppenheimer approximation [55]. Thus, in classical molecular dynamics, while using a potential function to describe molecular interactions, the kinetic energy contribution to the internal energy is simply the translational motion of the molecules. If the simulation models molecules with individual atoms, then the translational energy of the atoms account for the translational, rotation, and vibrational energy of the molecules.

$$E_k\left(\vec{p}^N\right) = \sum_i \frac{1}{2} m_i v_i^2 \tag{2.37}$$

All other forms of thermodynamic sensible energy, such as electron translation, electron spin, and nuclear spin, are accounted for in the potential energy function.

$$U_{P.E.}\left(\vec{r}^{N}\right)=\sum_{I<J}\sum U_{P.E.}\left(r_{ij}\right) \tag{2.38}$$

So, as stated in section 2.2, the total internal energy for an isolated system is defined by:

$$E_{T}\left(\vec{r}^{N},\vec{p}^{N}\right)=\sum_{i}\frac{1}{2}m_{i}v_{i}^{2}+\sum_{I<J}\sum U_{P.E.}\left(r_{ij}\right) \tag{2.39}$$

Analysis of the microcanonical ensemble (fixed number of particles, volume, and energy) using statistical thermodynamics reveals that the absolute temperature of a pure substance is proportional to the average kinetic energy [56].

$$k_{b}T=\frac{2}{3n}\left\langle E_{k}\right\rangle \tag{2.40}$$

Here, k_{b} is Boltzmann's constant, T is the absolute temperature, and n is the number of particles.

Pressure, assuming a pairwise additive potential, is obtained from the ideal gas law and the virial equation of state [48].

$$P=\frac{2n}{3V}\left\langle E_{k}\right\rangle-\frac{1}{3V}\left\langle\sum_{i<j}\sum r_{ij}\frac{dU_{P.E.}\left(r_{ij}\right)}{dr_{ij}}\right\rangle \tag{2.41}$$

where V is the volume. The first term on the right hand side is the ideal gas contribution, and the second term is the virial contribution, which accounts for intermolecular interactions.

The constant volume heat capacity is a measure of how the internal energy changes due to an isometric change in temperature and can be calculated by the expression:

$$C_v = \frac{1}{k_b T^2} \left\langle \left(E_T - \langle E_T \rangle \right)^2 \right\rangle \tag{2.42}$$

Here, $E_T - \langle E_T \rangle$ represents the fluctuation of the internal energy about its average value.

2.9 Summary

The basic underling methods used in molecular dynamics simulations to model and predict material response to external stimuli have been discussed. The fundamental equations of motion of Newton and Hamilton were developed and related to the motion of atoms. A brief discussion of intermolecular potential functions and their connection to Newton's second law was given. The fundamental governing equations of molecular motion were derived and converted into a finite difference form that is suitable for molecular dynamics simulations. Also, various boundary conditions and initial conditions were highlighted. A short, yet sufficient discussion about calculating system properties was given. In this discussion, equations for kinetic, potential, and total internal energy, temperature, pressure, and constant volume heat capacity were shown.

Although these methods are simple in nature, they are an extremely valuable tool to the scientist or engineer attempting to gaze into the sub-macroscopic world of material behavior.

CHAPTER 3

MOLECULAR DYNAMICS SIMULATIONS OF LASER INDUCED SHOCK RESPONSE OF REACTIVE NICKEL-ALUMINUM LAMINATED THIN FOILS

3.0 Introduction

To characterize the self-propagating, high-temperature exothermic alloying reactions of Ni/Al nanoscaled multilayered films induced by laser pulse shock loading, classical molecular dynamics simulations were performed. In the current work, a novel technique was developed to facilitate the energy input and distribution into nanolaminate thin films. The laser pulse shock loading technique enables the initial shock response of the material to be captured as well as the late-time mass diffusion controlled alloying reaction and Ni_3Al formation. Shock compression raises the temperature, pressure, and density of the Ni and Al layers which triggers the Ni to diffuse into the Al and initiate the self-propagating alloying reaction. Thermodynamic states, enthalpy of reaction, and global reaction rates of the laminated films were obtained. It was determined that the series of complex rarefaction and reflection waves play a significant role in altering the thermodynamic state of the laminate. Attributes of the rarefaction and reflection waves are controlled by the geometry and thickness of the alternating layers. The dependence of layer thickness on the temperature, pressure, enthalpy of reaction, and global reaction rate was investigated and characterized.

Numerous efforts have been carried out to develop accurate empirical intermolecular potentials of the Ni/Al binary system [6-8]. Fortunately, the success of these efforts has lead to the wide spread use of molecular dynamics to investigate the Ni/Al system. Previous molecular dynamics simulations using these potentials have

characterized the thermodynamics of the Ni/Al system [11, 14, 16]. Molecular dynamics

simulations have been performed to investigate the role that pressure and material voids

play in the alloying reaction process [16, 17]. Although results of prior work have been

verified indirectly through experiment, there has been little effort to develop a simulation

model that can be directly verified through experiment. The laser pulse modeling

approach offers a realizable system that, with minimal effort, could be configured into an

experiment. Figure 3.1 shows a schematic of an experimental configuration of a
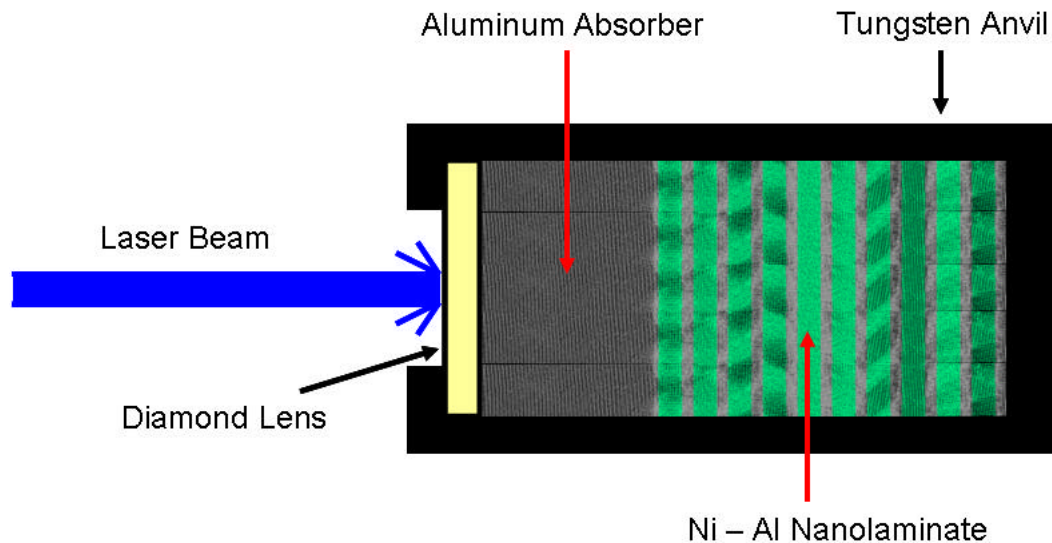
nanolaminated thin film system.

Figure 3.1 - A schematic that illustrates the physical system that is modeled with the laser pulse shock loading technique in the current work.

3.1 Simulation Approach

Classical molecular dynamics simulation methods, with an embedded-atom-

method (EAM) potential, are used to investigate the SHS reaction that results in the

formation of Ni_3Al. The simulation results, particularly the enthalpy of reaction,

adiabatic combustion temperature, and density, are compared to experimental data to validate the simulation methods.

The simulations were carried out using the Large-scale Atomic/Molecular Massively Parallel Simulator (LAMMPS) software package [57]. It was developed at Sandia National Laboratories, a US Department of Energy (DOE) facility, with funding from the DOE. It is an open-source code, distributed freely under the terms of the GNU Public License (GPL). The simulations require 3.25 days running on 125 single core 1.66GHz Intel Itanium processors to complete one nanosecond of simulation time.

3.2 The Embedded-Atom-Method Interatomic Potential

The majority of previous molecular dynamics modeling efforts involving the Ni/Al system have used the EAM potential parameters developed by Mishin *et al* to simulate the atomic interactions [6]. It was pointed out in [16] that these potential parameters are inadequate for predicting melting temperatures of the individual Ni and Al species. A more accurate description of Ni/Al interactions, using the Finnis-Sinclair EAM potential [58], was developed by Angelo, Moody, and Baskes [7] using empirical data from Chen [59, 60] and was employed in this work. Here, the energy of atom i embedded in the host is a function of the energy required to embed atom i plus one-half times the sum of the short-range pairwise interactions. Note that all atoms are viewed as being embedded in the host consisting of all other atoms.

$$E_i = F_a\left(\sum_{i \neq j} q_a(r_{ij})\right) + \frac{1}{2}\sum_{i \neq j} f_{ab}(r_{ij}) \tag{3.1}$$

Here, a and ß are atom species, r_{ij} is the separation distance between atoms i and j, $?_a$ is the contribution to the electron charge density from atom j at the location of atom i but

without atom i actually being present, $\boldsymbol{f_{ab}}$ is the short-range pairwise potential function, and F_a is an embedding function that represents the energy required to place atom i of type a into the electron cloud.

Like the Lennard-Jones potential function, the EAM potential is an approximation that describes the energy state of atoms. However, unlike the Lennard-Jones potential, which is purely pairwise additive, the EAM and its variants are multibody potentials. The multibody structure of the potential comes from the electron charge density contribution term. As stated above, $?_a$ is the contribution to the electron charge density at the location of atom i from atom j. It can be shown that the electron charge density contribution at the location of atom i from atom j strongly depends on the configuration of neighboring atoms. Thus, the energy level between atom j and atom i is not independent of all other atoms and therefore termed multibody dependant. Consequently, these models are particularly well suited for metallic systems where atoms are in close proximity to one another.

Seven functions are required to fully define the EAM potential for binary alloy systems such as Ni/Al. Three of the functions define pairwise interactions (Ni-Ni, Al-Al, Ni-Al), Two of them describe the embedding process, and the last two functions represent the electron cloud contributions. These functions can be established empirically from the physical properties of the solids or from detailed quantum chemistry calculations. The functions used for the current simulations are stored in a tabularized format and interpolated by splines.
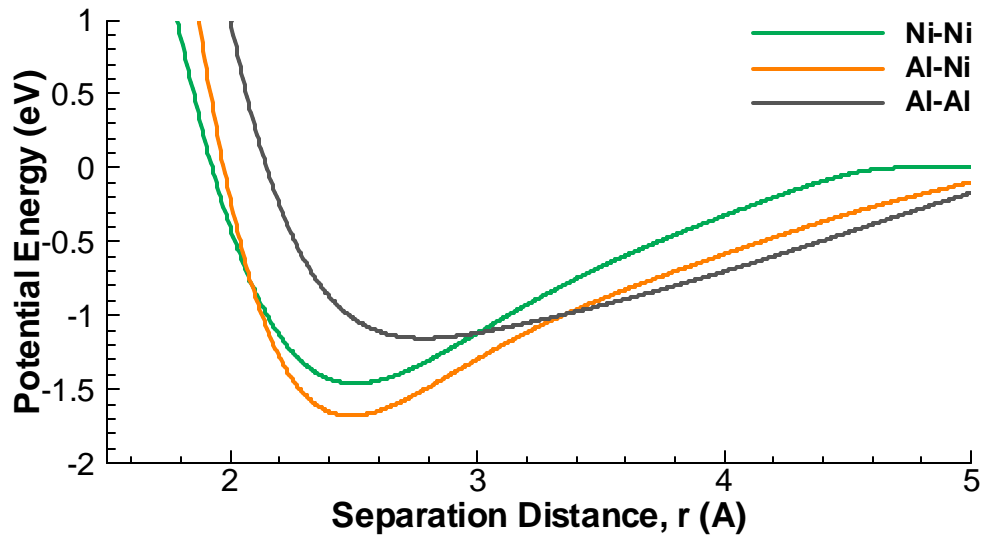
Figure 3.2 - Potential energy functions used to define pairwise interactions between Ni and Al for the EAM potential defined by Angelo *et al* [7].
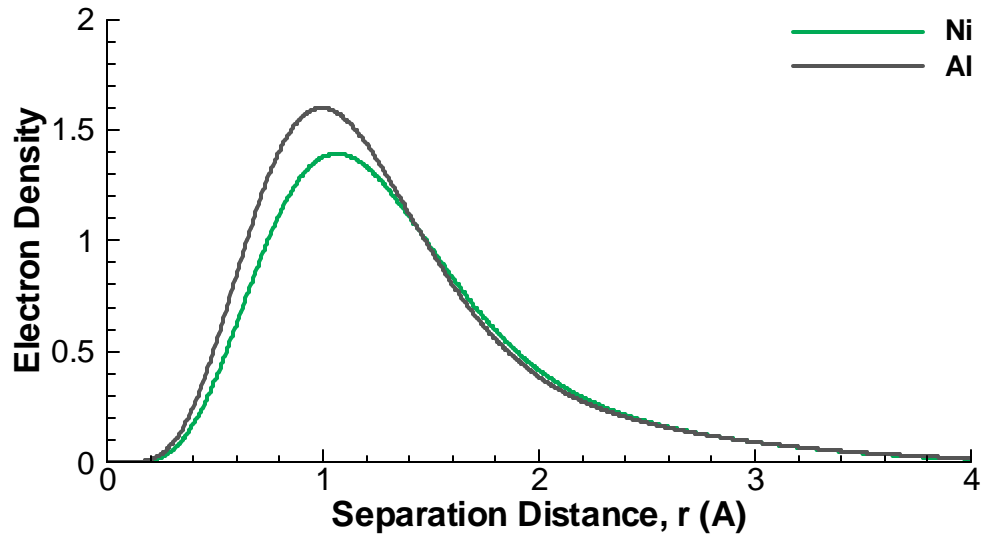

Figure 3.3 - Functions used to define the electron density for the EAM potential defined by Angelo *et al* [7].
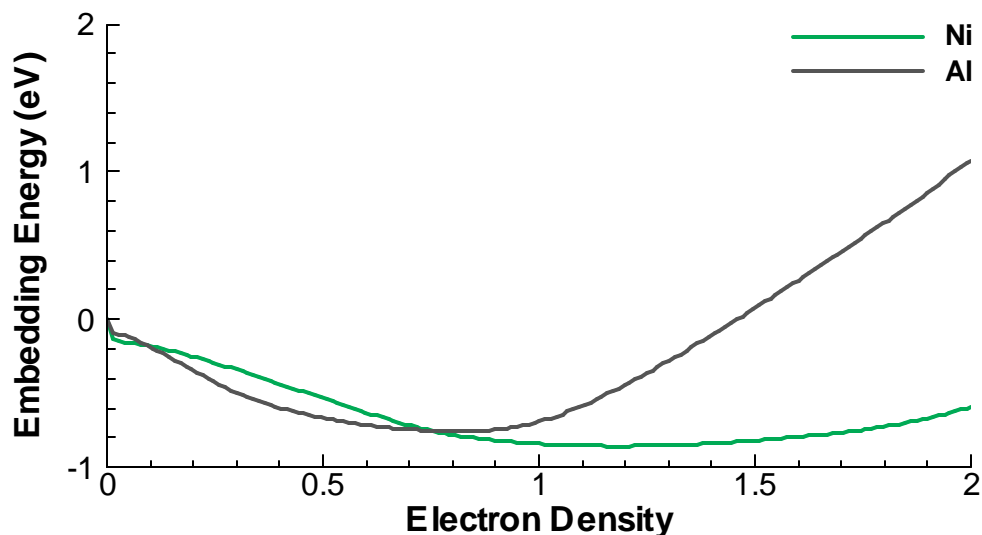
Figure 3.4 - Embedding functions used to define the embedding process for the EAM potential defined by Angelo _et al_ [7].

Figures 3.2 through 3.4 show the seven input functions (tabulated data sets) that define the EAM potential that is employed by LAMMPS for the current investigation. It is interesting that, like all natural chemical processes, the SHS alloying reaction is driven by energy minimization. Figure 3-2 shows that the lowest energy well occurs for Ni-Al interactions at a separation distance of about 2.5 Å.

This potential model accurately predicts the thermodynamic states during the solid-liquid phase transition of the Ni, Al, and Ni_3Al species, which is of significant importance for calculating the enthalpy of reaction for the given systems in this work.

3.3 Initial Configuration and System Equilibration

In total, three simulations were performed. Each simulation consists of approximately 775,000 atoms that are arranged in alternating Ni/Al layers. Additionally, the dimensions of each system are 888 Å in the Y coordinate, 100 Å in the X coordinate,

and 100 Å in the Z coordinate. The laminate is configured in such a way to ensure that each bilayer has 3 Ni atoms for every Al atom. Thus, a 3 Ni to 1 Al overall ratio in the laminated region is guaranteed. The first simulation is comprised of 12 total layers, 6 layers of each metal species. The layer thicknesses in the first simulation are approximately 65 Å and 30 Å for Ni and Al, respectively. The second simulation contains 20 total layers, 10 layers of each metal species and the thicknesses of the Ni and Al layers are 36 Å and 18 Å, respectively. The third simulation features layer thicknesses for Ni and Al equal to 26 Å and 12 Å, respectively. This simulation features 28 total layers, 14 layers of each metal species. Figure 3.5 shows a comparison of the three geometries. Each simulation contains a thick aluminum region that precedes the laminate. The role of the thick aluminum region is to absorb the energy given off by the laser pulse. Because the aluminum absorption region is long and continuous, a nice planner shock wave forms. Compressive heating, due to shock wave interactions, acts as the trigger mechanism for the exothermic alloying reaction.
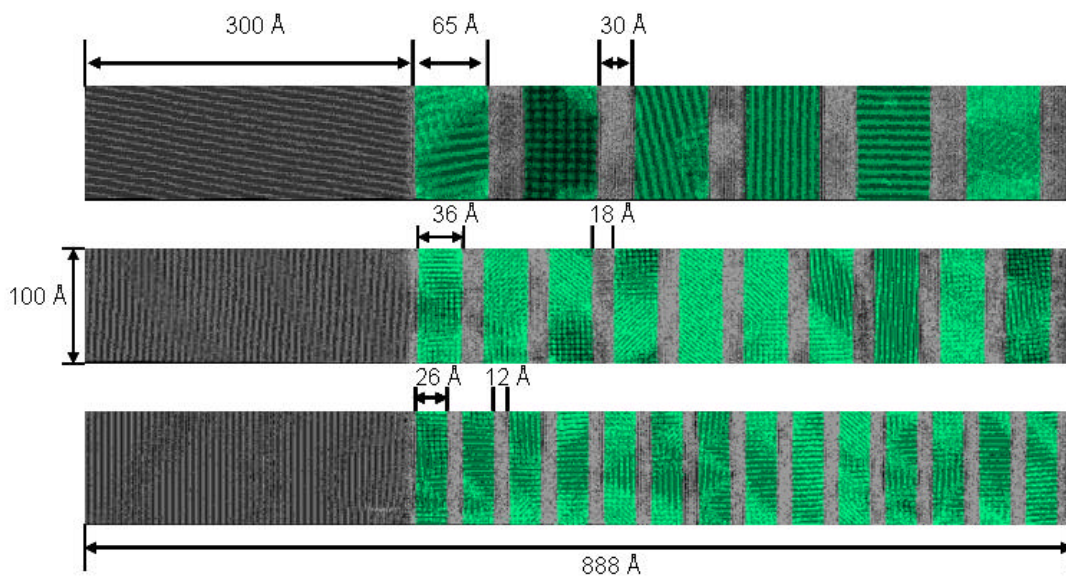

Figure 3.5 - A schematic depicting the relative geometric differences of the three molecular dynamics simulations performed in the current work.

To monitor the time evolution of the localized system properties, the sample was discretized along the Y coordinate into 180 fixed cells, each with dimensions of 4.93 Å by 100 Å by 100 Å. After the initial shock compression, each cell is comprised of approximately 3,500 to 5,500 atoms, depending on the compression state and Ni concentration. The cell properties are obtained by averaging over all the atoms within the cell. The properties that are calculated within each cell are the kinetic, potential, total (internal) energies, pressure, temperature, enthalpy, number density, and mass fraction (concentration).

At the outset of the simulation, the system was initialized at 0 K before being equilibrated to 300 K. The equilibration process was carried out by rescaling the atom velocities using a Gaussian distribution. During this stage of the simulation, periodic boundary conditions were used in the X (into the page) and Z coordinates. A shrink-wrapping boundary condition was used in the Y coordinate to allow the system to expand while being equilibrated to room temperature. After the atom velocities were rescaled such that the system temperature reached 300 K, an additional simulation without any system constraints was performed and the energy levels were monitored to ensure thermodynamic equilibrium.

3.4 Laser Pulse Heat Addition

This work features an innovative modeling technique that was specifically developed to facilitate the energy input and distribution into the nanolaminate film. The laser pulse shock loading technique enables the initial shock response of the material to be captured as well as the late-time mass diffusion controlled alloying reaction and Ni_3Al

formation. This technique uses a laser pulse to rapidly heat the aluminum energy absorber. In turn, the rapid heating of the aluminum produces a planner shock wave that propagates through the entire sample and triggers the SHS alloying reaction. Figure 3.6 shows a pressure and temperature contour of the shock wave formation and initial propagation.
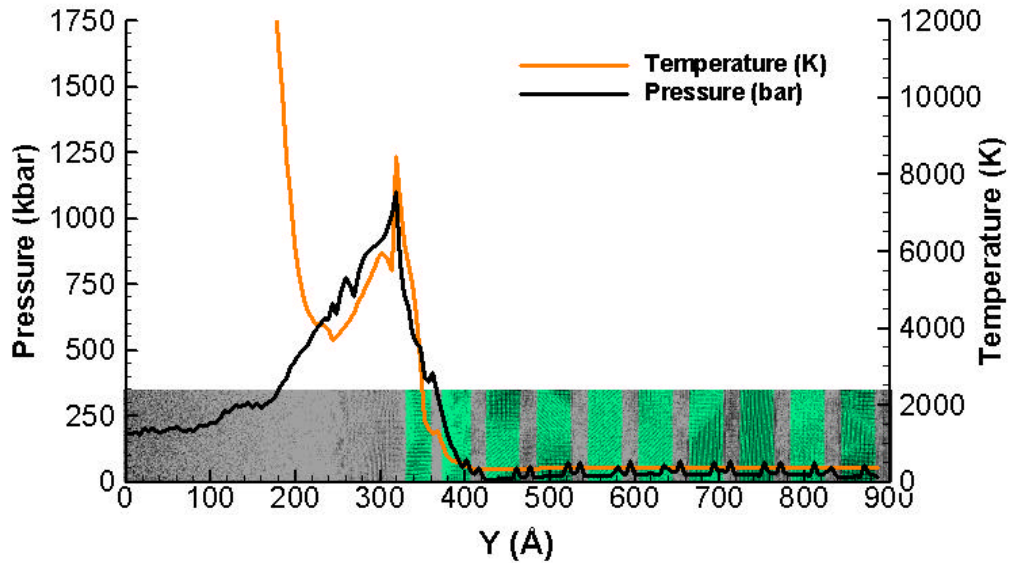

Figure 3.6 - A temperature and pressure contour plot that captures the initial shock wave formation and propagation.

3.4.1 Laser Pulse Characteristics

The characteristics of the laser pulse used in the current study were obtained from experimental efforts conducted by Juhasz, Smith, Metha, Harris, and Bron. In [61], an experimental arrangement, using a CW pumped, actively mode-locked, Nd: YAG master oscillator and a Kiton Red gain dye, was configured to produce a laser that is tunable between 590 nm to 645 nm and delivers 3 ps duration pulses at 80mW. It is assumed for the current model that the 3 ps laser pulse has a wavelength equal to 645 nm and a power output of 80 mW.

3.4.2 Transient Absorption of Laser Radiation

The output intensity of a YAG laser pulse on the fs to ps timescale is usually

treated with a Gaussian distribution because the temporal intensity distribution often

takes a hyperbolic-secant-squared pulse shape [61]. The laser output intensity is then

expressed as:

$$I(t) = \frac{I_0}{\sqrt{p}\, t_p} \exp\left[-\left(\frac{t}{t_p}\right)^2 \right] \tag{3.2}$$

where t_p is the characteristic time of the laser pulse and I_0 is the laser intensity which is

defined as the total energy carried by the laser pulse per unit cross section of the laser

beam. The distribution of transient absorbed energy density is expressed by an

exponential absorption law [62].

$$Q(x,t) = \frac{(1 - R_{sf})}{d} \exp\left(-\frac{x}{d}\right) I(t) \tag{3.3}$$

$$Q(x,t) = \frac{(1 - R_{sf}) I_0}{d \sqrt{p}\, t_p} \exp\left[-\frac{x}{d} - \left(\frac{t}{t_p}\right)^2 \right] \tag{3.4}$$

where d is the material absorption depth and R_{sf} is the surface reflectivity. This

expression represents the pulse energy source in the film. The material absorption depth

is a function of material type and incident wavelength. The wavelength of the laser pulse

in air is 645 nm. The wavelength of the laser pulse changes as it travels through different

medium. Changes in wavelength for the given system are governed by (3.5) and (3.6).

$$N_{Air}\, l_{Air} = N_C\, l_C \tag{3.5}$$

$$N_C\, l_C = N_{Al}\, l_{Al} \tag{3.6}$$

where N is the refractive index and λ is the wavelength. It was determined that N_{Air}, N_C, and N_{Al} are equivalent to 1.002926, 2.650000, 1.110000 at wavelengths λ_{Air}, λ_C, and λ_{Al} of 645 nm, 243.47 nm, and 582.64 nm, respectively [63]. The laser intensity I_0 and reflectance R_{sf} of the aluminum surface are determined from the reflectance and transmittance.

$$R_{sf} = \left[\frac{N_1 - N_2}{N_1 + N_2} \right]^2 \tag{3.7}$$

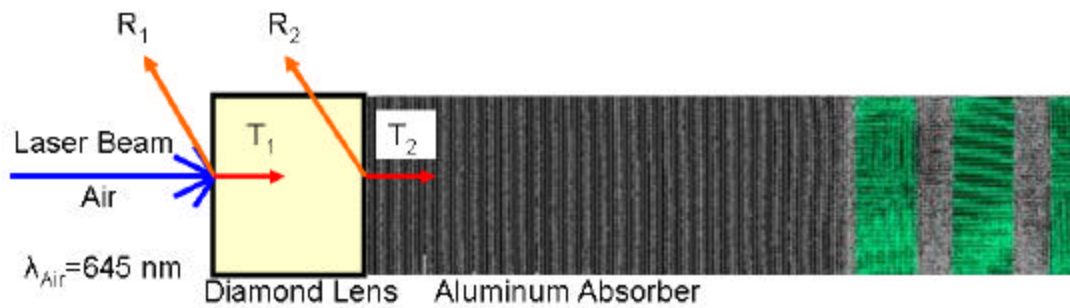$$T_{sf} = \frac{4N_1 N_2}{(N_1 + N_2)^2} \tag{3.8}$$

Figure 3.7 - A schematic depicting the change in laser beam properties as the pulse penetrates different material layers.

Work done by Hagemann, Gudat, and Kunz in [64] shows that aluminum, at a wavelength of 582.64 nm, has an absorption depth of 66.7 Å ($d = 1/\mu$). The distribution of transient absorbed energy density is plotted in Figure 3.9 for values of $t_p = 3$ ps, $R_{sf} = 0.16775$, $I_0 = 1909.8$ J/m^2, $d = 66.7$ Å.
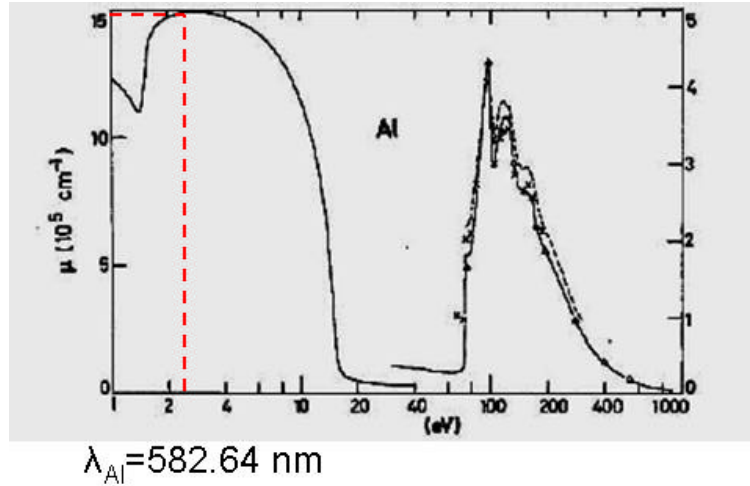
λ_{Al}=582.64 nm

Figure 3.8 - Data from Hagemann *et al* [64 was used to determine the absorption depth of the laser pulse in aluminum (d=1/μ).
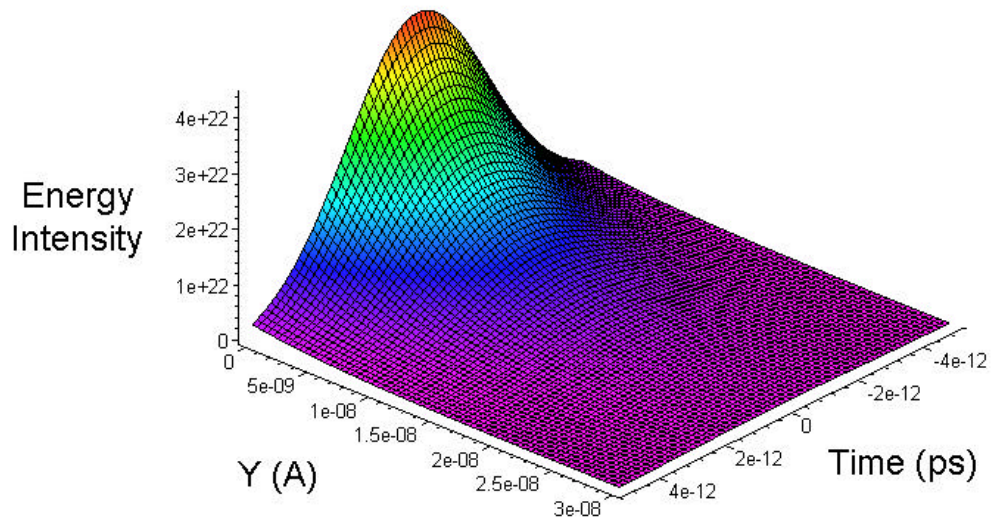

Figure 3.9 - Absorbed energy density distribution in the aluminum absorber due to the 3 ps laser pulse.

Here, Y=0 signifies the diamond-aluminum surface. The plot shows that most of the energy is absorbed within the first 150 Å of the aluminum absorber. The timescale was chosen for simplicity, -3.0 ps on the plot corresponds to the simulation time of 120 ps, which is the beginning of the laser heating portion of the simulation. The temperature as

49

a function of space and time is obtained from the integration of (3.4) and serves as the energy input mechanism for the molecular dynamics simulation. The ensemble of atoms that make up the aluminum absorber is partitioned into several groups. Each group of atoms is heated at a rate that corresponds to the temperature profile obtained form the integration of (3.4). Again, the group temperatures are controlled by rescaling their velocities with a Gaussian distribution.

3.4.3 Boundary Conditions and Justifications

A change in boundary conditions is necessary in order to effectively model the combustion synthesis process. Boundary conditions in the X and Z coordinates remain periodic. Fixed, perfectly reflective boundary conditions are used in the Y coordinate. The fixed, perfectly reflective boundary condition on the right side of the system models the interactions between the system and the tungsten anvil depicted in Figure 3.1. The boundary condition on the left side is also fixed and perfectly reflective. It models interactions between the system and the diamond lens. The fixed, perfectly reflective boundary condition does not allow any mass or energy to transfer across the boundary. The application of a perfectly reflective boundary condition at the aluminum-tungsten interface can be justified by investigating the shock wave physics at the material boundary. Figure 3.10 shows a simple system where the initial shock wave is traveling through the aluminum and impacts the material interface. Here, shock waves are assumed to be square waves with no attenuation and are represented by the bold arrows. The material interface shown in the x-t diagram is represented by the dotted line. Note that the tungsten anvil has a much higher shock impedance (density times the sound speed) than aluminum. When the initial shock reaches the material interface, a shock

wave is transmitted into the tungsten and another shock wave is reflected back into the aluminum. All three shock waves have different speeds as indicated by the different slopes shown in the x-t diagram. The areas shown on the x-t diagram are called fields and represent thermodynamic states of the materials. The pressure and particle velocities are equivalent within each field.
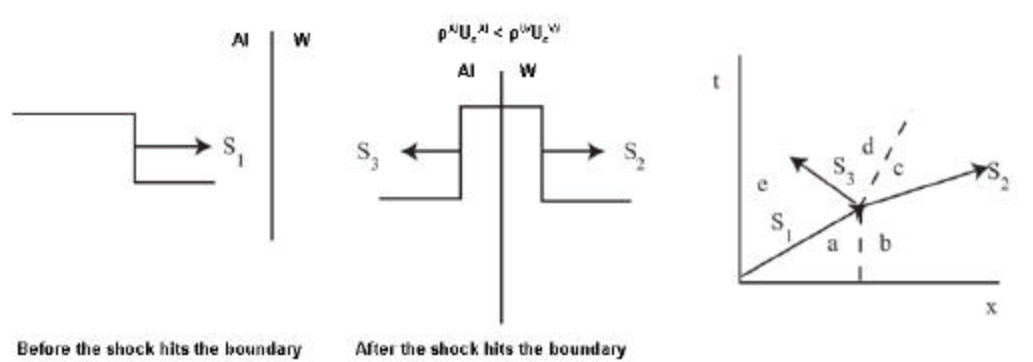

Figure 3.10 - (Left) Depiction of a square shock wave traveling towards the Al-W interface. (Center) The shock impacts the interface which produces a shock reflection back into the Al material. (Right) The corresponding Al-W x-t diagram. (The figure was taken from [65]).

Impedance matching is a commonly used solution technique to calculate the pressure magnitudes of the transmitted and reflected shock waves at material boundaries [65]. Additionally, this method is used to calculate particle motion of the fields shown on the x-t diagram. The pressure versus particle velocity curves (Hugoniots) of the aluminum-tungsten boundary system are plotted in Figure 3.11 for initial shock wave pressures of 80 and 25 GPa. According to shock wave physics, to conserve mass, momentum, and internal energy, shock waves must produce states that fall on the forward or backward facing Hugoniot P-u_p curves [65]. Note that when a shock wave crosses a material boundary the pressures and particle velocities of both materials must be the equivalent.

51

The only point where this condition is met is where the reflected aluminum Hugoniot curve intersects the forward facing tungsten Hugoniot curve (at states c and d). For an initial shock pressure of 80 GPa, the reflection off of the tungsten surface produces a pressure of 153 GPa, just 4% lower than the pressure produced from a perfect reflection. For an initial shock pressure of 25 GPa, the reflection off of the tungsten surface produces a pressure of 46 GPa, just 8% lower than the pressure produced from a perfect reflection. Thus, it is demonstrated that the perfectly reflective boundary applied to the aluminum-tungsten interface predicts the reflected shock wave pressure reasonably well for high and relatively low initial shock wave pressures.

A less desirable result is obtained when this analysis technique is applied to the boundary condition that models the aluminum-diamond interface. Because diamond has a much lower density than tungsten, and therefore lower shock impedance than tungsten, the slope of its forward facing Hugoniot is much lower. Figure 3.12 shows the Hugoniot P-u_p plot of the aluminum-diamond interaction. This result shows that for initial shock pressures of 80 GPa and 25 GPa the perfectly reflective boundary condition over predicts the reflected shock pressures by 63% and 61%, respectively.
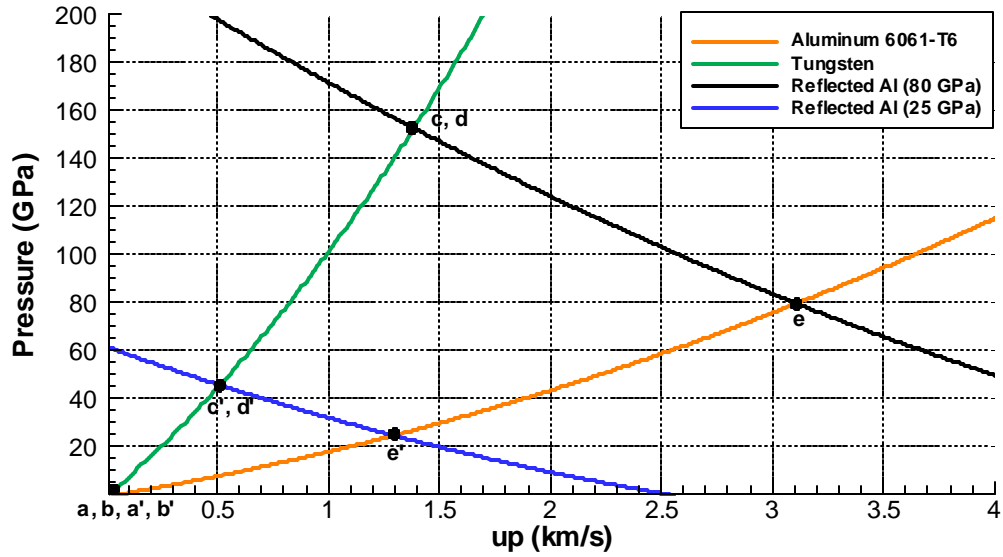
Figure 3.11 - Shock Hugoniot plots representative of a shock wave impacting an Al-W interface. (The shock Hugoniot data was obtained from [66]).
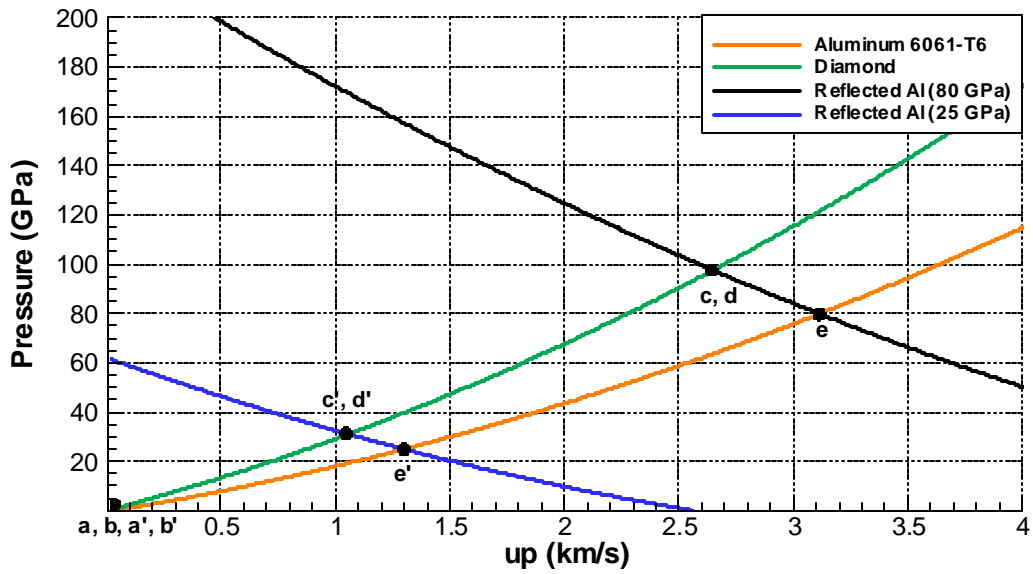

Figure 3.12 - Shock Hugoniot plots representative of a shock wave impacting an Al-C$_{\text{Diamond}}$ interface. (The shock Hugoniot data was obtained from [66]).

However, the over prediction of reflected shock wave pressure at the left

boundary has a minimal effect on the global process, especially in the laminated region.

As the shock wave travels through the system it transfers energy to the atoms via collisions. Figure 3.13 shows that the peak pressure of the shock wave rapidly reduces during the first oscillation period. This implies that the shock wave has delivered most of its energy to the system during this period. It is interesting to note that most of the energy of the shock wave is expended in the laser pulse absorption region that is comprised of superheated aluminum. In fact, the peak pressure has been reduced to such a relatively small value by the time the shock reflects off the diamond-aluminum interface that over predicting the shock reflection by 63% is insignificant. Additionally, the energy that the system would loss by applying more accurate boundary conditions is extremely small in comparison to the total system energy. Thus, the application of the perfectly reflective boundary conditions for the given model is justified.
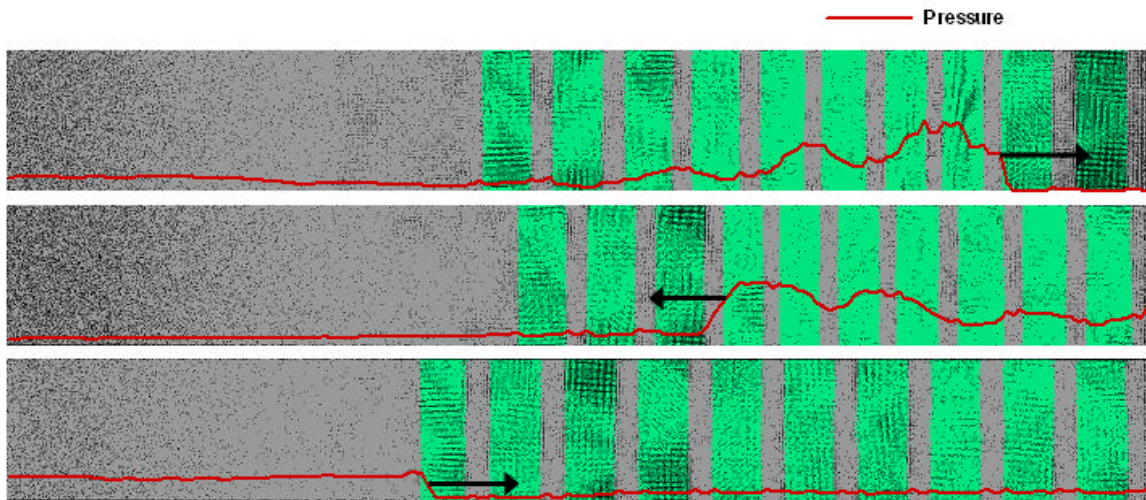

Figure 3.13 - Snapshots of the shock wave traveling through the system during the first oscillation period.

3.5 Constant NVE Molecular Dynamics Simulation

After the 3 ps laser pulse has delivered its energy to the system, the simulation is transitioned into a molecular dynamics simulation where the number of atoms, system

volume, and system energy are held constant (NVE). Here, the boundary conditions are equivalent to the boundary conditions used in the laser pulse heat addition portion of the simulation. Figure 3.14 shows a plot of the kinetic, potential, and total energy of the entire system versus time. This plot demonstrates that the total system energy is conserved during this phase of the simulation.
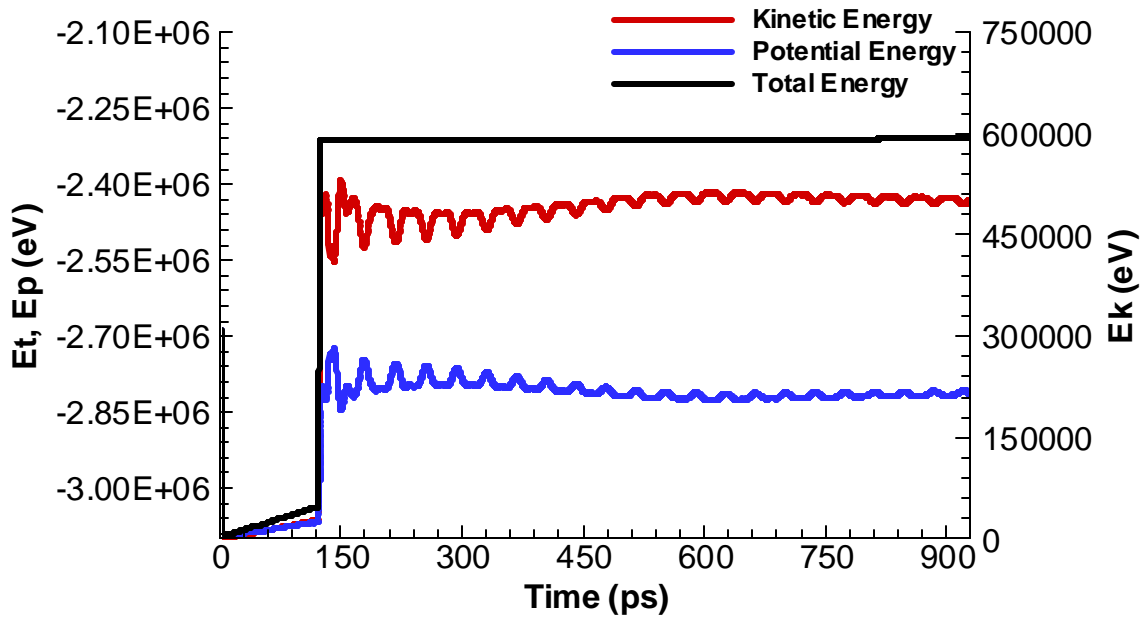

Figure 3.14 - Kinetic, potential, and total energy of the entire 10 bilayer system.

3.5.1 Monitoring System Properties

Local thermodynamic properties are calculated from the history cells shown in Figure 3.15 for the 10 bilayer simulation. The locations of these cells were chosen to be far from the laser absorption region so that the reaction characteristics could be studied without influence of the superheated aluminum, yet far enough away from the aluminum-tungsten interface to avoid boundary effects.
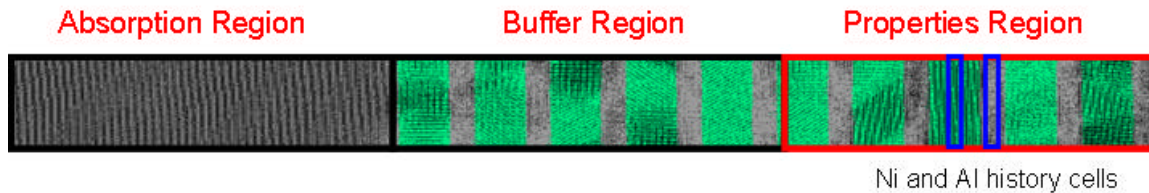
Figure 3.15 - Locations of the Ni and Al history cells in the 10 bilayer sample used for calculating thermodynamic and reaction properties.

Once the initial shock wave has traveled through the first period (the length of the system and back), a series of complex rarefaction and reflection waves, as well as mechanical forces, begin to dominate the system response and trigger the alloying reaction. The system undergoes a continuous series of compression and expansion periods, which cause further heating of the metal layers. This accordion-like compression-expansion behavior of the nanolaminate is the source of oscillatory fluctuations in local thermodynamic properties. Due to the fixed nature of the history cells and the oscillatory motion of the system, special care needs to be taken in the analysis of the local thermodynamic properties. Figure 3.16 shows the pressure-time history plotted on top of the number of atoms-time history for the Al history cell. Close inspection of this plot reveals that the thermodynamic properties are representative of Al in an expanded state and nickel in a compressed state. It should be noted that the history cells are only 4.8 Å wide and when in a compressed state, the width of the thinnest Al layer is less then 4.8 Å. Thus, in order to obtain thermodynamic data that is representative of pure Al, this work uses the thermodynamic data in expanded states. Data that is representative of pure, individual chemical species is crucial for calculating accurate enthalpy of reaction data.
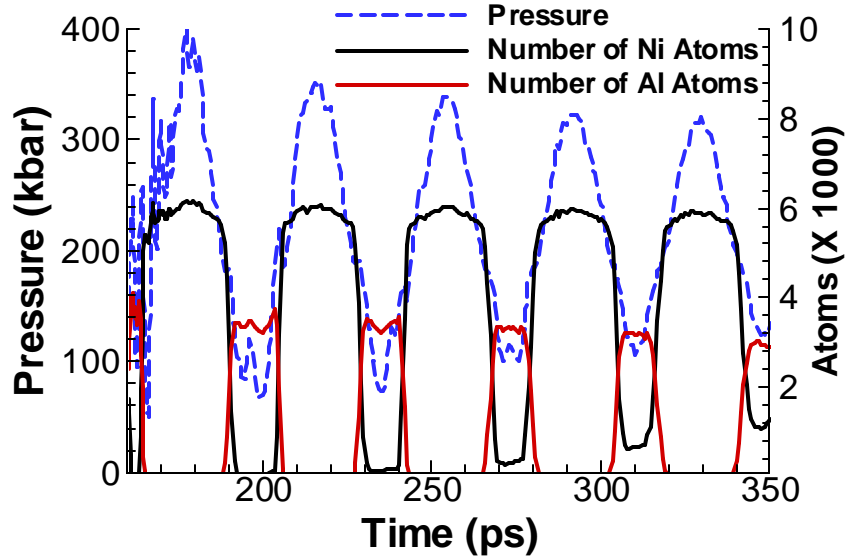
Figure 3.16 - Pressure-time history plotted on top of the number of atoms-time history for the Al history cell. This plot demonstrates that the thermodynamic output is representative of Al in an expanded state and Ni in a compressed state.

3.6 System Response of the 10 Bilayer Simulation

3.6.1 Calculating Thermodynamic Properties

This section is intended to provide a simple overview of how the thermodynamic properties shown in this section were calculated. A more in depth discussion was given in chapter 2. A consequence of explicitly modeling individual atomic interaction is that the translational energy of the atoms account for the translational, rotation, and vibrational energy of the molecules. Thus, the kinetic energy is calculated from:

$$E_k\left(\vec{p}^N\right) = \sum_i \frac{1}{2} m_i v_i^2 \qquad (2.37)$$

The potential energy is obtained from the sum of the EAM interatomic potential that was discussed in detail in section 3.2 [7].

$$\sum_{i=1}^n E_i = \sum_{i=1}^n \left[F_a\left(\sum_{i\neq j} q_a\left(r_{ij}\right) \right) + \frac{1}{2} \sum_{i\neq j} f_{ab}\left(r_{ij}\right) \right] \qquad (3.1)$$

So, as stated in section 2.2, the total internal energy for an isolated system is defined by:

$$E_T\left(\vec{r}^N, \vec{p}^N\right) = \sum_i \frac{1}{2} m_i v_i^2 + \sum_i E_i \qquad (2.39)$$

Recall from section 2.8 that the temperature is related to the average kinetic energy from:

$$k_b T = \frac{2}{3n}\langle E_k \rangle \qquad (2.40)$$

The pressure is calculated from the trace of the stress tensor, which is defined by:

$$S_{ab} = -m v_a v_b + \frac{1}{2}\sum_{n=1}^{N_p}\left(r_{1a}F_{1b} + r_{2a}F_{2b}\right) - \frac{1}{2}\sum_{n=1}^{N_b}\left(r_{1a}F_{1b} + r_{2a}F_{2b}\right) - \frac{1}{3}\sum_{n=1}^{N_a}\left(r_{1a}F_{1b} + r_{2a}F_{2b} + r_{3a}F_{3b}\right)$$

$$- \frac{1}{4}\sum_{n=1}^{N_d}\left(r_{1a}F_{1b} + r_{2a}F_{2b} + r_{3a}F_{3b} + r_{4a}F_{4b}\right) - \frac{1}{4}\sum_{n=1}^{N_i}\left(r_{1a}F_{1b} + r_{2a}F_{2b} + r_{3a}F_{3b} + r_{4a}F_{4b}\right) - \sum_{n=1}^{N_f} r_{ia}F_{ib}$$

$$(3.9)$$

The first term is a kinetic energy contribution for atom i. The second term is a pairwise energy contribution where n loops over the N_p neighbors of atom i, r_1 and r_2 are the positions of the 2 atoms in the pairwise interaction, and F_1 and F_2 are the forces on the 2 atoms resulting from the pairwise interaction. The third term is a bond contribution of similar form for the N_b bonds which atom i is part of. There are similar terms for the N_a angle, N_d dihedral, and N_i improper interactions atom i is part of. Finally, there is an optional term for the applied internal constraint forces.

The enthalpy is calculated by:

$$\Delta H = \Delta E_T + V\Delta P \qquad (3.10)$$

3.6.2 Thermodynamic Response and Reaction Rate

Further inspection of Figure 3.16 shows that at 200 ps no Ni atoms have migrated into the history cell and at 235 ps, one oscillation period later, the Ni has started to diffuse into the Al. Thus, the alloying reaction begins at 200 ps. Figure 3.17 shows five snapshots of the 10 bilayer molecular dynamics simulation that captures the initial configuration, combustion synthesis wave propagation, and final Ni_3Al intermetallic formation. The figure also depicts reaction initiation and propagation stemming from both ends of the laminated region. The combustion synthesis wave on the left side of the laminate is initiated from the extremely high temperature of the superheated aluminum laser energy absorber. The reaction on the right side of the laminate is initiated from the shock wave reflection at the aluminum-tungsten interface. Due to the impedance mismatch at the interface, the pressure in the Al doubles for a short period of time. This high pressure peak causes the temperature to spike which, in turn, accelerates the diffusion of the Ni species in the local region. Figure 3.18 shows that the initial shock wave reaches a peak pressure of over 1,000 kbar. It also reveals that the pressure in the expanded Al gradually increases from 92 kbar to 175 kbar as the reaction progresses. Similarly, the temperature in the Al increases from 1,000 K to 2,400 K during the alloying reaction process, which matches well with the experimental range of 1873 K to 2573 K, reported by Sikka and Deevi [39].
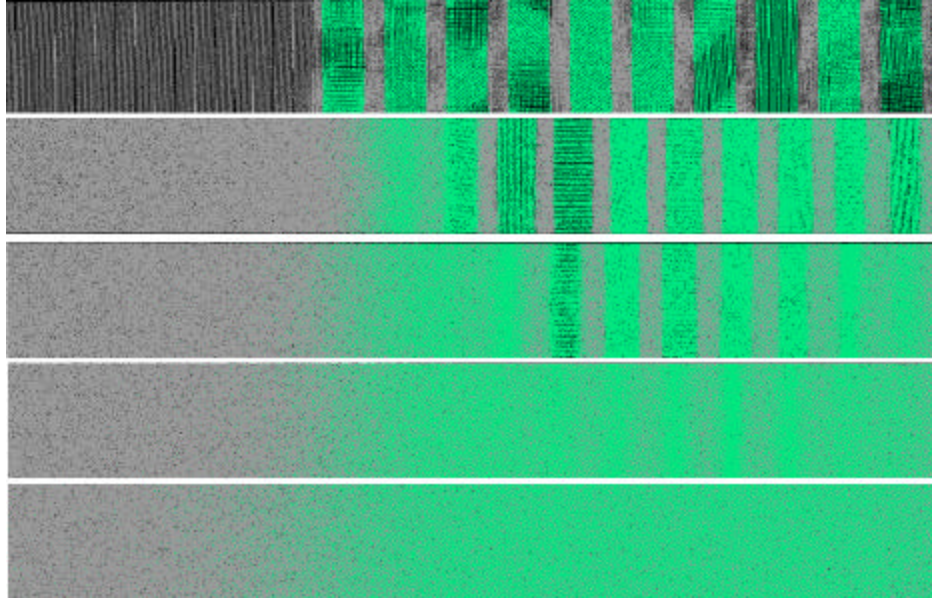
Figure 3.17 - Snapshots in time illustrating the combustion synthesis wave propagation and final Ni₃Al product formation.
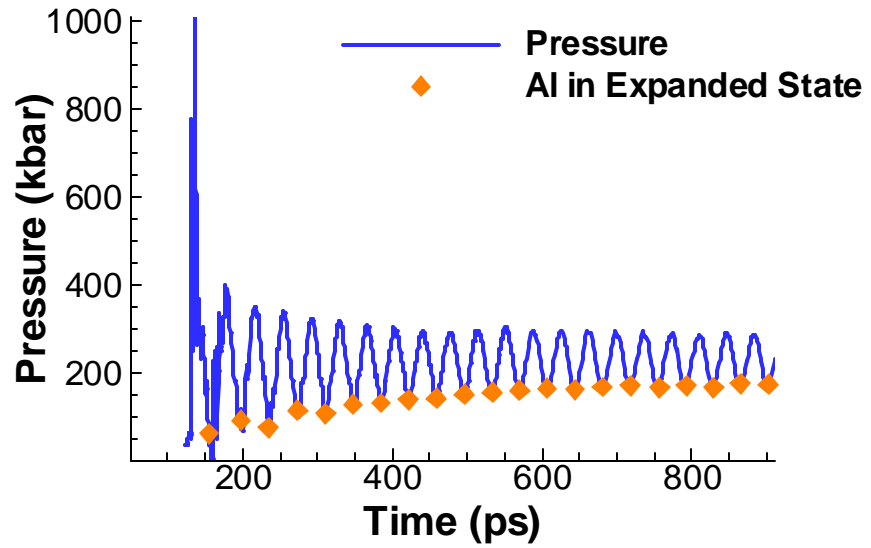

Figure 3.18 - Pressure -time history of the Al history cell defined in Figure 3.15.
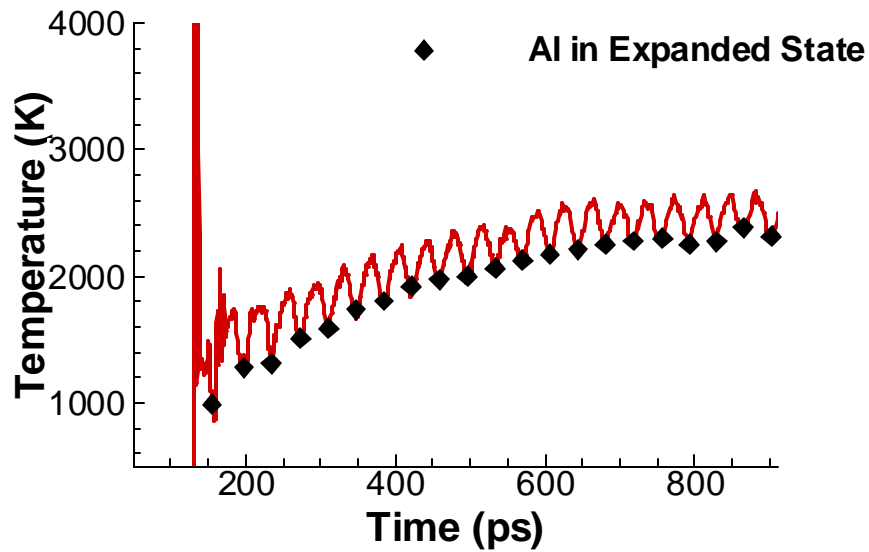
Figure 3.19 - Temperature-time history of the Al history cell defined in Figure 3.15.

The Ni migration into the cell and the Al migration out of the cell are monitored by tallying each species at every expansion period (Figure 3.20). Also, to investigate the global reaction rate, the Ni-to-Al ratio is calculated and is plotted in Figure 3.21. This figure demonstrates that for the given energy input mechanism, the 10 bilayer system has a global reaction rate of about 600 ps. e.g. the entire laminated region of Ni and Al reacts to form the product Ni_3Al within 600 ps. The initial and final (NVE) density contours are shown in Figure 3.22 and serve as further evidence of Ni_3Al formation. The figure shows the existence of a large density gradient in the forward section of the laminate. This is due to the large Ni concentration gradient between the laminate and the Al absorber region. It also shows the existence of a small density gradient near the aluminum-tungsten interface. The final density of the material within the history cells (700 Å-800 Å) is approximately equal to 7.33 g/cc, which is consistent with the accepted value of 7.26 g/cc for Ni_3Al [36].
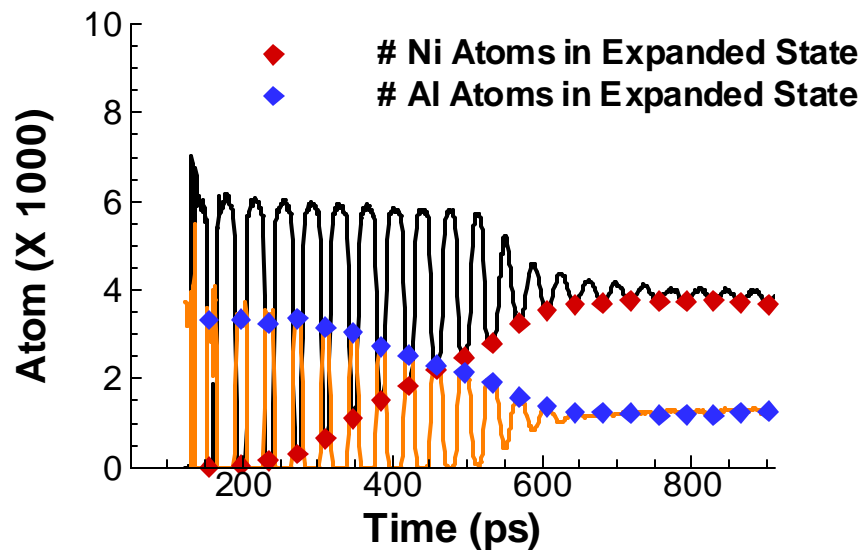
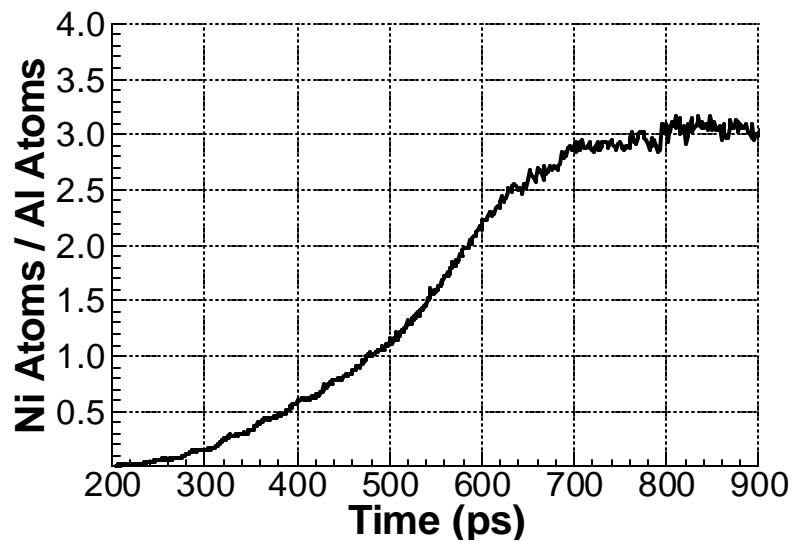**Figure 3.20 - Atom species-time history of the Al history cell defined in Figure 3.15.**

Figure 3.21 - Ni-to-Al atom ratio-time history of the Al history cell defined in Figure 3.15.
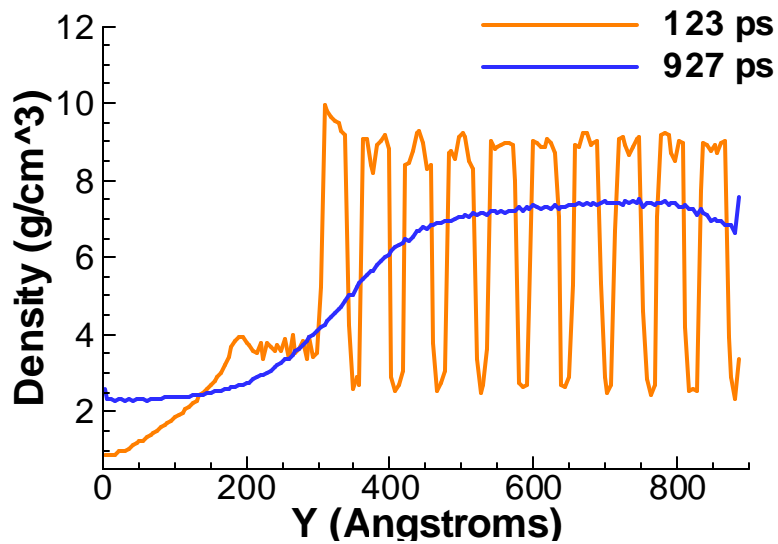
Figure 3.22 - Density contours of the initial and final 10 bilayer system configurations. A large gradient exists at the left side due to the pure aluminum energy absorber. A smaller gradient exists on the right side due to the boundary. Local thermodynamic properties are calculated between 700 Å and 800 Å.

3.6.2 Constant Volume Process

During the first 70 ps of the NVE simulation, the laminated region undergoes two shock loading oscillation periods. During this initial loading phase, each layer experiences significant plastic deformation and energy transfer. However, after the first two loading periods, the laminated region displays elastic behavior. Due to the perfectly reflective boundary condition at the aluminum-tungsten interface, the layer volumes return to their same values during the expansion phase of each oscillating period. Therefore, very little mechanical energy is being transferred to each bilayer. Additionally, any temperature gradients that exist across bilayers are very small and can be neglected. Thus, after the initial loading period, there is zero net energy transfer to each bilayer and a constant volume process can be assumed in going from one expanded state to another expanded state in time.

63
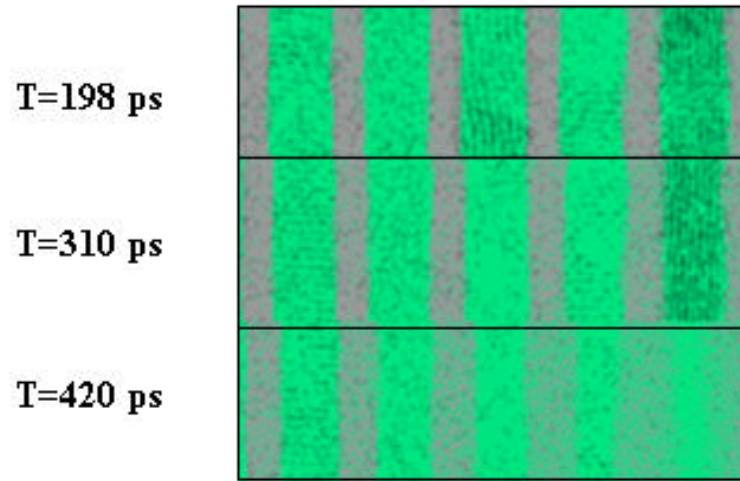
Figure 3.23 - Snapshots in time of the right end of the laminate demonstrate that after the initial loading period, the volumes of the bilayers remain constant.

3.6.3 Enthalpy of Reaction

The enthalpy of reaction is calculated using enthalpy values, for all species, in expanded states. The enthalpies of the reactants, Al and Ni, are obtained from Figures 3.24 and 3.25 at a time of 197 ps. The enthalpy of Ni_3Al is obtained from Figure 3.24 at a time of 901 ps (note that this value could be obtained form either figure). The temperature and pressure values of the Al at 197 ps are used as the reference state for the calculation and are listed in Table 3.1.

Figure 3.24 - Enthalpy-time history of the Al history cell defined in Figure 3.15.

Figure 3.25 - Enthalpy-time history of the Ni history cell defined in Figure 3.15.

65

For incompressible substances, both the constant-pressure and constant-volume specific heats are identical [67].
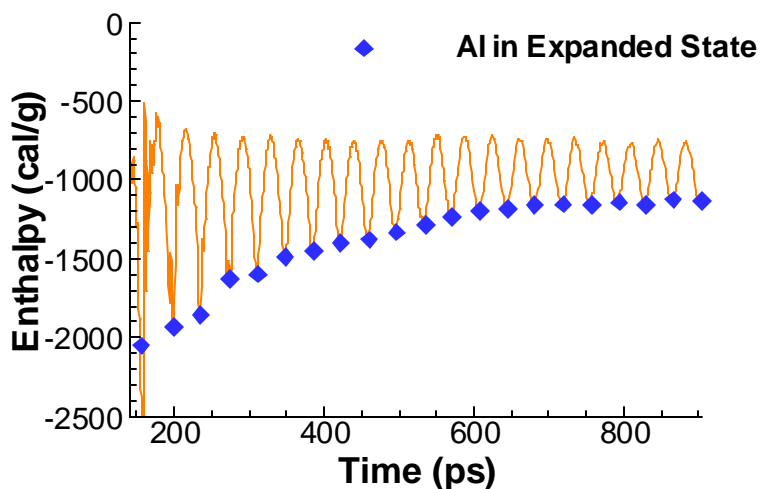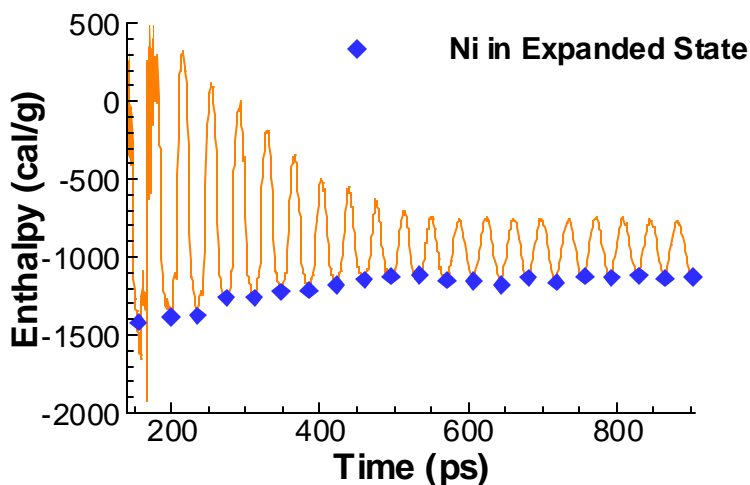
$$C_v \cong C_p \equiv C \tag{3.10}$$

The change in internal energy and enthalpy of incompressible substances that undergo phase change from a solid to liquid are given by:

$$\Delta U = \int_{T_1}^{T_m} C_s(T)dT + \Delta H_m + \int_{T_m}^{T_2} C_l(T)dT \tag{3.11}$$

$$\Delta H = \Delta U + V\Delta P \tag{3.12}$$

$$\Delta H = \int_{T_1}^{T_m} C_s(T)dT + \Delta H_m + \int_{T_m}^{T_2} C_l(T)dT + V\Delta P \tag{3.13}$$

Thus, for the reaction

$$3Ni + Al \rightarrow Ni_3Al \tag{3.14}$$

the enthalpy of reaction is given by:

$$\Delta H_{RXN} = H_{\mathrm{Prod}} - H_{\mathrm{Reac}} \tag{3.15}$$

where

$$H_{\mathrm{Prod}} = 1 \cdot \overline{h}_{Ni_3Al} \tag{3.16}$$

$$H_{\mathrm{Reac}} = 1 \cdot \overline{h}_{Al} + 3 \cdot \overline{h}_{Ni} \tag{3.17}$$

$$\overline{h}_{Ni_3Al} = \overline{h}_{Ni_3Al}^{T_{ref},P_{ref}} - \left[\int_{T_{Ni_3Al}^{ref}}^{T_{Ni_3Al}^{m}} C_{p,s}^{Ni_3Al} dT + \Delta \overline{h}_{Ni_3Al}^{m} + \int_{T_{Ni_3Al}^{m}}^{T_{Ni_3Al}} C_{p,l}^{Ni_3Al} dT + V\left(P_{Ni_3Al} - P_{Ni_3Al}^{ref}\right) \right] \tag{3.18}$$

$$\overline{h}_{Al} = \overline{h}_{Al}^{T_{ref},P_{ref}} \tag{3.19}$$

$$\overline{h}_{Ni} = \overline{h}_{Ni}^{T_{ref},P_{ref}} + \int_{T_{Ni}}^{T_{Ni}^{ref}} C_{p,s}^{Ni} dT + V\left(P_{Ni}^{ref} - P_{Ni}\right) \tag{3.20}$$

From (3.9) through (3.19), along with the thermodynamic data listed in Table 3.1 and Table 3.2, the enthalpy of reaction, ΔH_{RXN}, is calculated to be -151.93 kJ mol^{-1}, which is in good agreement with experiment.[40, 46, 47]

Table 3.1 – Reference data of initial and final thermodynamic states used to calculate the enthalpy of reaction for the system containing 10 bilayers.

Species	Time (ps)	Temperature (K)	Pressure (kPa)	Cell Volume (m^3)	Ni Atoms	Al Atoms	Enthalpy (kJ mol^{-1})
Al	197.25	1283.88	9182238.00	4.9333E-26	43	3351	-192.41
Ni	197.25	1273.96	8994668.00	4.9333E-26	5353	0	-336.88
Ni$_3$Al	901.50	2391.69	17506430.00	4.9333E-26	3735	1222	-945.73

Table 3.2 – Thermodynamic data[68, 69] used for calculating the enthalpy of reaction. Table was taken from [46].

Species	T$_m$ (K)	ΔH_m (kJ mol^{-1})	Specific Heat Capacity (J mol^{-1} K^{-1})
Ni	1728	17.6	$C_{p,s} = 32.60 + 1.80 \times 10^{-3}T - 5.58 \times 10^5 T^{-2} (T = 298K - 630K)$
			$C_{p,s} = 29.68 + 4.18 \times 10^{-3}T - 9.32 \times 10^5 T^{-2} (T = 630K - 1728K)$
			$C_{p,l} = 38.87$
Al	933	10.9	$C_{p,s} = 20.65 + 12.37 \times 10^{-3}T$
			$C_{p,l} = 31.77$
Ni$_3$Al	1668	50.0	$C_{p,s} = 88.49 + 32.22 \times 10^{-3}T + 0.001 \times 10^5 T^{-2} - 0.001 \times 10^{-6}T^2$
			$C_{p,l} = 142.00$

3.7 Concentration and Diffusion Coefficient

The oscillatory nature of this system presents difficulties in calculating the diffusivity directly. Instead, diffusivity is studied by relating the calculated Ni concentration to viscosity functions that are correlated to experiment [21]. In turn, the diffusion coefficient is obtained from the viscosity through the Stokes-Einstein equation.

This approach has many shortcomings and as a whole, lacks completeness. One drawback to this approach is that there is little chance that simulation results would be consistent with the viscosity correlations (i.e. it is unclear if the atoms in the simulation

really behave in a way that is described by the viscosity correlation). Another drawback

of this approach is that the experimental data may contain error that is not accounted for

by the viscosity correlations (measuring viscosity of molten metals is not a trivial task).

Even though this approach has many shortcomings and may lack accuracy, it does

give valuable insight into the diffusion process of this system. The goal of this section is

to provide a qualitative understanding of the diffusion mechanisms that drive the

chemical alloying reaction. Figure 3.26 shows the Ni mass fraction (concentration)

versus the special coordinate, Y and time for a small portion of the domain in the 10

bilayer system. The plot is representative of the Ni concentration of a single Al layer

packed in between two one-half layers of Ni. The plot also shows the temperature

contour plotted on top of the concentration surface. Here, the concentration data is

obtained from the simulation data. It is interesting that, initially, the diffusion mechanism

is controlled by the erosion of the Ni interface and that the Al fails to penetrate the solid

Ni lattice. However, it is observed that as the remainder of the Ni lattice melts (t~500 ps)
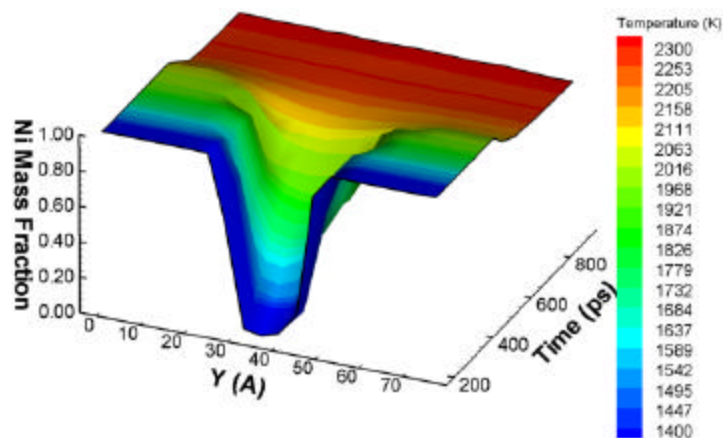
Al rapidly diffuses into the Ni regions.

Figure 3.26 - Ni mass fraction versus length and time of a layer of Al packed between two one-half layers of Ni. The temperature contour is plotted on top of the Ni mass fraction surface.

It was demonstrated through experiment that the viscosity of the Ni/Al binary system behaves according to the Arrhenius law (experiments were conducted at temperatures up to 2100 K) [21].

$$\boldsymbol{m}(\boldsymbol{c}_{Ni}, T) = \boldsymbol{m}_{\infty}(\boldsymbol{c}_{Ni}) \cdot \exp\left(\frac{E_a(\boldsymbol{c}_{Ni})}{RT}\right) \tag{3.21}$$

where R is the gas constant and T is the absolute temperature. Here, the asymptotic viscosity, μ_8, and the activation energy, E_a, depend on the Ni concentration, $\boldsymbol{c}_{Ni}$. With the Ni concentrations obtained from the molecular dynamics simulation results, the viscosity for the Ni/Al binary system is defined with (3.20). The diffusion coefficient, D, is obtained from the Stokes-Einstein relation.

$$D = \frac{k_b T}{6 \boldsymbol{pm} \cdot r_{Ni}} \tag{3.22}$$

$$D = \frac{k_b T}{6 \boldsymbol{pm}_{\infty}(\boldsymbol{c}_{Ni}) \exp\left(\frac{E_a(\boldsymbol{c}_{Ni})}{RT}\right) r_{Ni}} \tag{3.23}$$

where k_b is Boltzmann's constant and r_{Ni} is the Ni atomic radius. Figure 3.27 shows a plot of the diffusion coefficient versus Ni concentration for various temperatures. Figure 3.28 shows a plot of the diffusion coefficient versus the special coordinate Y and time. This plot demonstrates that there is a lot of variation in the diffusion coefficient, especially early in time when Ni concentration gradients are high. Although there is much variation locally, the overall range in diffusivity is somewhat small. The diffusion coefficient ranges form 0.00 Å^2/ps to 0.75 Å^2/ps over the entire system during the 900 ps of simulation time. Only a difference of 0.75 Å^2/ps exists between the area with the highest diffusivity and the area with the lowest diffusivity.
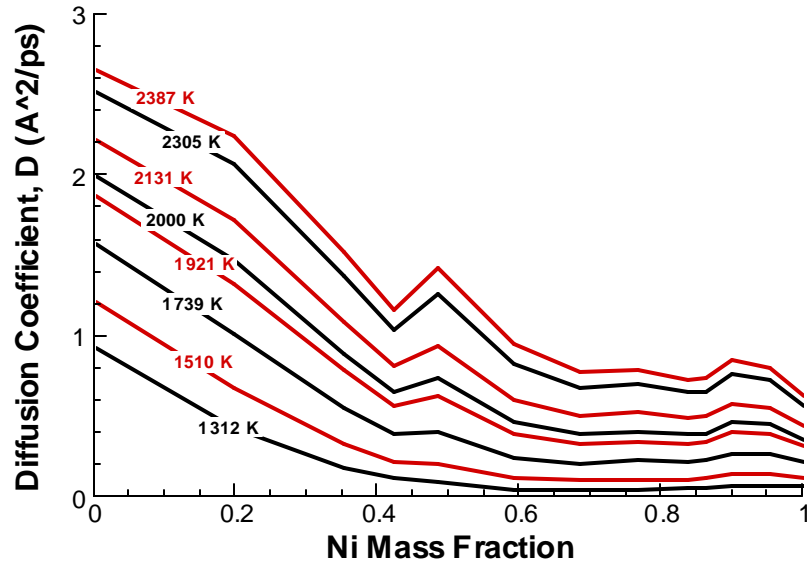
Figure 3.27 - The diffusion coefficient versus Ni mass fraction is plotted for various temperature values. Experimental data describing the viscosity as a function of Ni concentration from [21] was used to generate the curves.
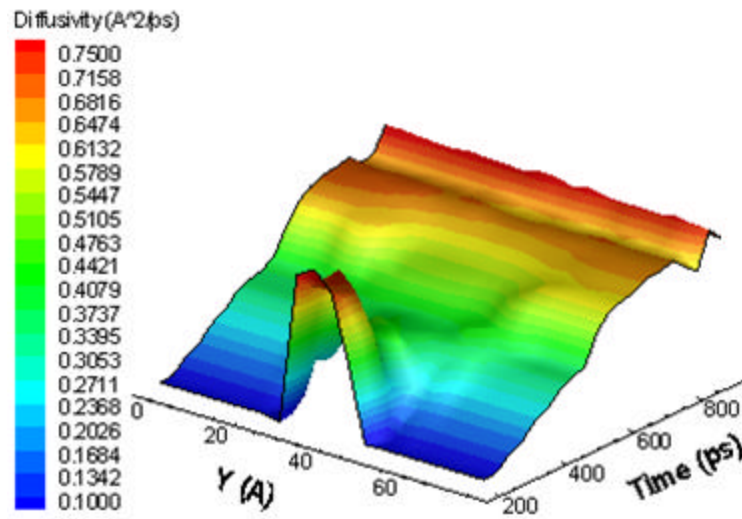

Figure 3.28 - Diffusion coefficient versus length and time for a layer of Al packed between two one-half layers of Ni.

3.8 Effects of Layer Thickness

Figure 3.29 shows that the system with 10 total bilayers reaches the highest pressure. The systems with 12 and 28 bilayers share a similar pressure rise in early time. In late time the system with 12 bilayers reaches a higher pressure than the system with 28 bilayers. The highly complex behavior of the shock wave reflections and system configuration makes it difficult to investigate trends in system pressure. Judging from Figure 3.29, it is unclear if any trend in pressure exists due to the layer thickness size. Figure 3.30 shows the temperature versus time comparison of the three systems. It is evident by comparing Figure 3.30 to Figure 3.31 that a correlation exists between temperature and reaction rate. The system with 28 total bilayers, and thus the smallest Ni and Al thicknesses, has the highest temperature early in time and possesses the fastest reaction rate, while the system with 12 bilayers, and thus the largest Ni and Al layer thicknesses, has the lowest early time temperature and the slowest reaction rate. All three systems have a similar late-time reaction temperature, which is also shown in Figure 3.30. This result is somewhat intuitive due to the diffusion controlled nature of the reaction where larger layer thicknesses imply longer diffusion times and hence, slower reaction rates. Figure 3.32 shows the enthalpy of the Al for the three systems. Similarly, Figure 3.33 shows the enthalpy of the Ni for the three systems. The enthalpy-time histories are used to calculate the enthalpy of reaction of each of the three systems. The $?H_{RXN}$ values of the three systems all fall within the range of -173.82 ± 4.51 cal g^{1}, which demonstrates a good level of precession and accuracy [40, 46, 47]. Thus, it appears that the enthalpy of reaction is unaffected by the layer thickness size of the laminate.

Figure 3.29 - Pressure-time history comparison of the three simulations performed in this work. Data is taken from the Al history cells defined section 3.5.1.

Figure 3.30 - Temperature-time history comparison of the three simulations performed in this work. Data is taken from the Al history cell defined section 3.5.1.

Figure 3.31 - Reaction rate comparison of the three simulations performed in this work. Data is taken from the Al history cell defined section 3.5.1.

72
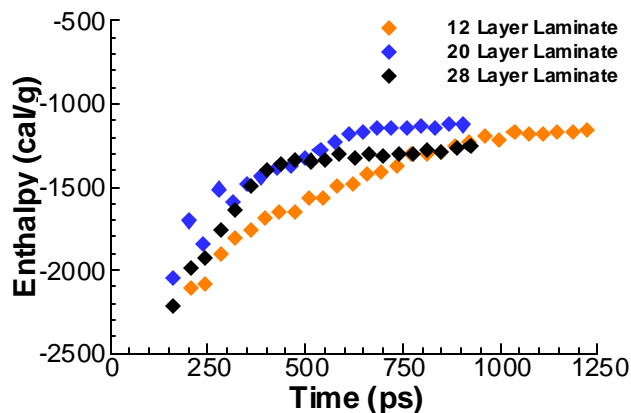
Figure 3.32 - Enthalpy-time history comparison of the three simulations performed in this work. Data is taken from the Al history cell defined section 3.5.1.

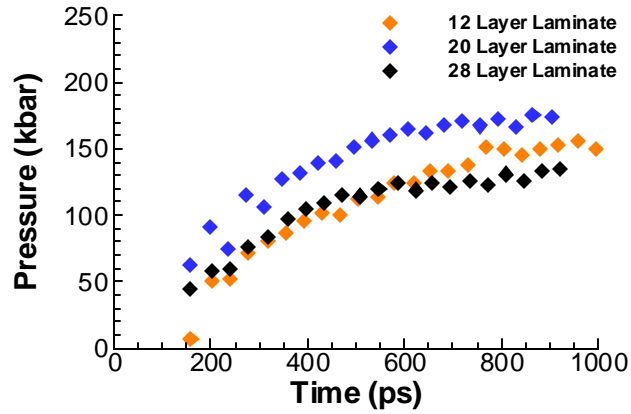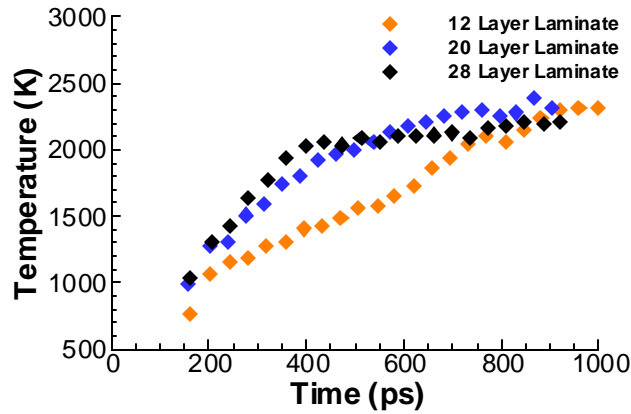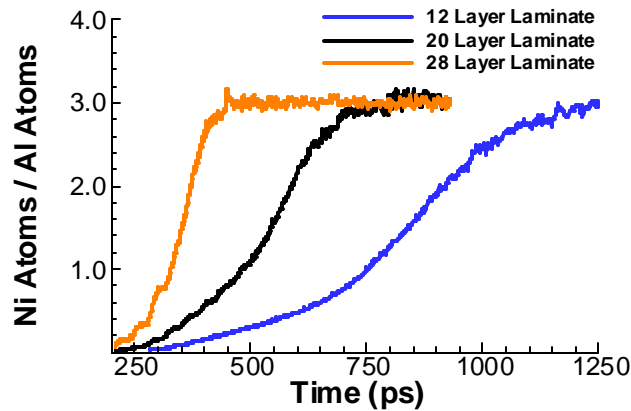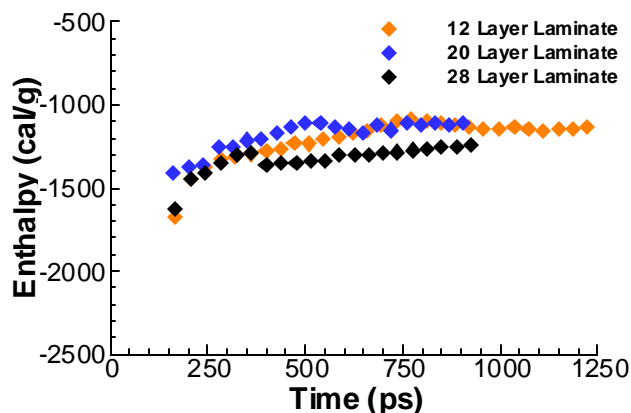**Figure 3.33 - Enthalpy-time history comparison of the three simulations performed in this work. Data is taken from the Ni history cell defined section 3.5.1.**

Table 3.3 - Reference temperatures and pressure used to calculate the enthalpy of reaction of each of the three systems. The adiabatic combustion temperatures are listed as well as the calculated enthalpy of reaction values.

Bilayer Thickness (Å)	T_{Ref} (K)	P_{Ref} (bar)	T_{Max} (K)	ΔH_{RXN} (cal g^{-1})
95	1066.92	51048.08	2497.11	-169.31
54	1283.88	91822.38	2391.69	-178.32
38	1306.17	58251.95	2252.83	-175.43

73

CHAPTER 4

CONCLUSIONS AND FUTURE WORK

4.0 Conclusions of Work

Classical molecular dynamics simulations, using an embedded-atom-method potential, were performed to investigate laser induced shock responses in reactive Ni/Al nanolaminates. An innovative technique was developed to facilitate the energy input and distribution into the nanolaminate systems. The laser pulse shock loading technique enables the initial shock response of the material to be captured as well as the late-time mass diffusion-controlled alloying reaction and Ni_3Al formation. In total three simulations, each with unique Ni and Al layer thicknesses, were completed. Using this modeling technique, important aspects of the self-propagating, high-temperature exothermic alloying reaction of the Ni/Al nanoscaled multilayered films were characterized.

Thermodynamic data, including temperature, pressure, density, enthalpy, and enthalpy of reaction was obtained for each simulation. Also, the global reaction rate of Ni_3Al formation was determined for each simulation. The temperature, density, and enthalpy of reaction results were compared to experimentally obtained data of Ni/Al reactions. It was shown that the initial densities of Ni and Al (8.86 g/cc and 2.63 g/cc, respectively) and final density of Ni_3Al (7.33 g/cc) compared well with measured results (8.908 g/cc, 2.70 g/cc, and 7.26 g/cc, respectively). The adiabatic combustion temperatures of the three systems, 2253 K, 2392 K, and 2497 K, all fall within the experimental range reported by Sikka *et al* [39]. Additionally, the enthalpy of reaction values obtained from simulation (-169.31 cal g^{-1}, -178.32 cal g^{-1}, and -175.43 cal g^{-1}),

compared well with experimentally determined values ranging from -180.0 cal g^{-1} to -183.0 cal g^{-1} reported by Barin *et al* and Varma *et al* [68, 69, 40]. These results were also used in a comparison study between the three simulations to detect the effects of layer thickness. Results from this study indicated that a trend exists between layer thickness and reaction rate, which correlated well with temperature rise. The system with the smallest bilayer thickness had the fastest reaction rate and highest early-time temperature rise; whereas the system with the largest bilayer thickness had the slowest reaction rate and lowest early-time temperature rise. The comparison study also showed that little variation in enthalpy of reaction exists among the three systems. Therefore, it was concluded that the bilayer thickness, in the range of 38 Å to 95 Å, has little influence on the amount of energy that is liberated by the Ni_3Al reaction.

A diffusion study, based on the Ni concentration of a single bilayer of the 10 bilayer simulation and correlated viscosity relations obtained from experiment, was performed. Results of this analysis revealed that, initially, the diffusion mechanism is controlled by the relatively slow erosion of the solid Ni interface. The results also showed that the Al atoms were unable to penetrate the Ni interface until melting occurred. It was determined that the diffusion coefficient has a range of only 0.75 $Å^2$/ps for the entire laminated region.

In many ways, the general results of this work support the description of the SHS diffusion controlled reaction mechanism given by Varma and Mukasyan [40]. It was demonstrated that aluminum melts and rapidly spreads around the solid Ni interface. It was shown that diffusion of the Ni species in molten Al is the limiting stage of the combustion process. One aspect of their description was not supported by the results

obtained in this work. No evidence was found that supports the existence of a layer, whose thickness remains constant during the reaction, comprised of the intermediate species $NiAl_3$ and Ni_2Al_3. With this aside, the results of this work strongly support their description of the Ni_3Al reaction.

4.1 Future Work and Concluding Thoughts

Although the current work provides a unique window into the atomistic processes that govern alloying reactions between Ni and Al, much more work is required in this field to obtain a fully characterized chemical reaction mechanism. Advancements in reactive force fields, particularly the ReaxFF potential model, have enabled molecular dynamicists to monitor the formation and destruction of chemical species by modeling the formation/destruction of individual chemical bonds. Even though ReaxFF molecular dynamics is much more labor intensive and requires more computational resources (due to the fact that each bond is accounted for at all times during the simulation), a detailed analysis of intermediate chemical species can be executed with accuracy. Thus, accurate formulations of complex chemical reaction mechanisms can be developed. This level of analysis would also provide the means to carry out a much more accurate diffusion study of the Ni/Al system. The current laser pulse shock loading technique, applied to a molecular dynamics simulation with the ReaxFF model, would provide the means of obtaining a fully characterized reaction mechanism of the Ni/Al system that could easily be validated with experiment. Additionally, other metallic systems of interest should be investigated using these methods. For example, their has been much interest expressed in the TiAl, TiNi, CuAl, and TiFe systems for various reasons, all of these systems could be

studied with these methods. In some cases, the macroscopic modelers have much to gain from these types of results. There is much interest in applying reactive burn models into Navier-Stokes/hydrocode type computer codes. It is of this author's opinion that, at this point in time, much is to be gained from applying these analysis methods to the H_2O/Al and H_3Al/H_2O systems.

REFERENCES

[1]   G. E. R. Schulze. Metallphysik, Akademie-Verlag, Berlin 1967

[2]   A. G. Merzhanov. In Particulate Materials and Processes: Advances in Powder Metallurgy and Particulate Materials. Princeton, NJ: Metal Powder and Industries Federation, 341 (1992)

[3]   A. Varma, A. S. Rogachev, A. S. Mukasyan, and S. Hwang. Advances in Chemical Engineering, 24, 79 (1998).

[4]   V. I. Itin and Y. S. Naiborodenko. High Temperature Synthesis of Intermetallic Compounds. Tomsk, Russia: Tomsk University Publishing (1989). (In Russian)

[5]   Y. Kaieda, M. Otaguchi, and N. Oguro. In Combustion and Plasma Synthesis of High-Temperature Materials, edited by Z. A. Munir and J. B. Holt. New York: VCH Publishers, 106 (1990)

[6]   Y. Mishin, M. J. Mehl, and D. A. Papaconstantopoulos. Physical Review B, 65 (2002).

[7]   J. E. Angelo, N. R. Moody, and M. I. Baskes. Modelling Simul. Material Science and Engineering. 3 (1995).

[8]   M. S. Daw and M. I. Baskes. Physical Review B. 29 (1984).

[9]   Y. Wang, Z. Liu, and L. Chen. Acta Materialia, 52 (2004).

[10]   J. D. Althoff, Dane Morgan, D. de Fontaine, M. D. Asta, S. M. Foiles, D. D. Johnson. Computational Materials Science 10 (1998).

[11]   M. Asta, D. Moran, J. Hoyt, B. Sadigh, J. Althoff, D. de Fontaine, S. Foiles. Physical Review B. 59 (1999).

[12]   Y. Hong, L. YongJun, C. Min, and GUO ZengYuan. Science in China Series G: Physics, Mechanics & Astronomy. 50 (2007).

[13]   N. S. Weingarten, W. D. Mattson, and B. M. Rice. Journal of Applied Physics. (SUBMITTED) (2009).

[14]   N. S. Weingarten, W. D. Mattson, A. D. Yau, T. P. Weihs, and B. M. Rice. Journal of Applied Physics. (SUBMITTED) (2009).

[15]   J. Wang, E. Besnoin, O. M. Knio, and T. P. Weihs. Acta Materialia. 52 (2004).

[16] B. J. Henz, T. Hawa, and M. R. Zachariah. Journal of Applied Physics,105, 124310(2009)

[17] S. Zhao, T. C. Germann, and A. Strachan. Journal of Chemical Physics, 125 (2006).

[18] S. Zhao, T. C. Germann, and A. Strachan. Physical Review B, 76 (2007).

[19] V. Tomar and M. Zhou. Materials Science Forum Vols. 465-466 (2004) pp. 157-162

[20] S. Mudry, V. Sklyarchuk, and A. Yakymovych. Journal of Physical Studies. 12 (2008).

[21] M. Kehr, M. Schick, W. Hower, and I. Egry. High Temperatures-High Pressures. 37 (2008).

[22] M. S. Petrushevskii, E. S. Levin, and P. V. Gel'd. Russian Journal of Physical Chemistry. 45 (1971).

[23] S. K. Das, J. Horbach, M. Koza, S. M. Chatoth, and A. Meyer. Applied Physics Letters. 86 (2005).

[24] E. Javierre, C. Vuik, F. Vermolen, and S. van der Zwaag. Journal of Computational and Applied Mathematics. 192 (2006).

[25] M. J. Rizvi, H. Lu, C. Bailey. Thin Solid Films. 517 (2009).

[26] J. Crank, The Mathematics of Diffusion, 2nd edition, Oxford University Press, Clarendon Press, Oxford, 1975.

[27] J. Crank, Free and Moving Boundary Problems, Oxford University Press, Clarendon Press, Oxford, 1984

[28] D. Shah and E. Lee, In Intermetallic Compounds, edited by J. H. Westbrook and R. L. Fleischer. Chichester: Wiley, 3, 297 (2002).

[29] N. S. Stoloff, In Intermetallic Compounds, edited by J. H. Westbrook and R. L. Fleischer. Chichester: Wiley, 3, 325 (2002).

[30] R. L. Fleischer, In Intermetallic Compounds, edited by J. H. Westbrook and R. L. Fleischer. Chichester: Wiley, 3, 351 (2002).

[31] G. T. Gray and T. M. Pollock, In Intermetallic Compounds, edited by J. H. Westbrook and R. L. Fleischer. Chichester: Wiley, 3, 361 (2002).

[32]   D. L. Anton, In Intermetallic Compounds, edited by J. H. Westbrook and R. L. Fleischer. Chichester: Wiley, 2, 3 (1995).

[33]   N. S.Stoloff and D. E. Alman. Material Science and Engineering, A144, 51 (1991).

[34]   B. V. Novozhilov. Proc. Academy Sci. USSR, Phys. Chem. Sect., 141, 836 (1961).

[35]   ASM Handbook Committee: ASM Handbook, vol. 3, Alloy Phase Diagrams, ASM INTERNATIONAL, Materials Park, OH, 2-49 (1999).

[36]   C. T. Liu and D. P. Pope, In Intermetallic Compounds, edited by J. H. Westbrook and R. L. Fleischer. Chichester: Wiley, 2, 36 (1995).

[37]   A. Bose, B. H. Rabin, and R. M. German. Pow. Metal. International., 20, 25 (1988).

[38]   D. B. Miracle and R. Darolia. In Intermetallic Compounds, edited by J. H. Westbrook and R. L. Fleischer. Chichester: Wiley, 2, 53 (1995).

[39]   V. K. Sikka and S. C. Deevi, In Intermetallic Compounds, edited by J. H. Westbrook and R. L. Fleischer. Chichester: Wiley, 3, 512 (2002).

[40]   A. Varma and A. S. Mukasyan, In Self-Propagating High-Temperature Synthesis of Materials, edited by A. A. Borisov, L. De Luca, and A. Merzhanov: Taylor & Francis, 17 (2002).

[41]   M. Hansen. Constitution of Binary Alloys, 2nd edition. New York: McGraw-Hill, 118 (1958).

[42]   V. V. Aledsandrov, M. A. Korchagin, and V. V. Boldyrev. Dokl. Phys. Chem., 292, 114 (1987).

[43]   A. M. Kanury. Metall. Tran., 23A, 2349 (1992).

[44]   G. Cao and A. Varma. Combust. Sci. Tech., 102, 181 (1994).

[45]   K. A. Philpot, Z. A. Munir, and J. B. Holt. J. Mater. Sci., 22, 159 (1987).

[46]   W. Liu and J. N. Dupont. Metallurgical and Materials Transactions A, 34 (2003)

[47]   J. Wang, E. Besnoin, A. Duckham, S. J. Spey, M. E. Reiss, O. M. Knio, and T. P. Weihs. Journal of Applied Physics, 95 (2004).

[48]   Haile, J. M. Molecular Dynamics Simulations Elementary Methods. Wiley-Interscience Publication (1992).

[49]   Serway, R. A., Physics for Scientists and engineers 4th edition. Saunder College Publishing (1996).

[50]   S. Labik and A. Malijevsky, Monte Carlo Simulations of the Radial Distribution Function af Fluid Hard Sphere., Mol. Phys., 42, 739 (1981).

[51]   Lennard-Jones, J. E. — Proc. Roy. Soc., 1924, v. A 106, p. 463.

[52]   L. Verlet, "Computer 'Experiment' on Classical Fluids. I. Thermodynamical Properties of Lennard-Jones Molecules," Phys. Rev., 159, 98 (1967)

[53]   L. K. Timothy and B. E. Bona, State Space Analysis, McGraw-Hill (1968).

[54]   A. R. Leach, Molecular Modeling Principles and Applications, Prentice Hall (2001).

[55]   M.Born and R. Oppenheimer. Zur Quantentheorie der Molekeln. Ann. Phys. (Leipzig) **84** (20), 457 (1927).

[56]   Hill, T., L., An Introduction to Statistical Thermodynamics, Dover1986.

[57]   S. J. Plimpton. Journal of Computational Physics, 117 (1995).

[58]   M. W. Finnis and J. E. Sinclair. Philosophical Magazine A, 50, 45-55 (1984)

[59]   S. P. Chen, D. J. Srolovitz, and A. F. Voter. J. Mater. Res. 4 62.

[60]   S. P. Chen, A. F. Voter, R. C. Albers, A. M. Boring, and P. J. Hays. J. Mater. Res., 5 (1990).

[61]   T. Juhasz, G. O. Smith, S. M. Mehta, K. Harris, and W. E Bron. IEEE Journal of Quantum Electronics. 25, July (1989).

[62]   D. W. Tang and N. Araki. J. Phys. D: Appl. Phys. 29 (1996).

[63]   Optical Society Of America, *Handbook of Optics, Vol. 2: Devices, Measurements, and Properties*, Second Edition, edited by M. Bass, McGraw-Hill (1994).

[64]   H. J. Hagemann, W. Gudat, and C. Kunz. Journal of the Optical Society of America, 65 (1975).

[65]   J. W. Forbes, Shock Wave Compression of Condensed Matter (In Publication).

[66]   Lasl Shock Hugoniot Data, S. P. Marsh Editor Los Alamos Series on Dynamic Material Properties, University of California Press. (1980)

[67]   Y. A. Cengel and M. Boles, Thermodynamics: An Engineering Approach., McGraw-Hill (2001).

[68]   I. Barin, O. Knacke, and O. Kubaschewski: Thermochemical Properties of Inorganic Substances: Supplement, Springer-Verlag, Berlin, 1977, pp. 489-490.

[69]   I. Barin and O. Knacke: Thermochemical Properties of Inorganic Substances, Springer-Verlag, Berlin, 1973, pp. 11 and 575.